HIGH-SPEED DIAGNOSTICS IN A NATURAL GAS-AIR ROTATING DETONATION ENGINE AT ELEVATED PRESSURE

A Thesis

Submitted to the Faculty

of

Purdue University

by

Christopher Lee Journell

In Partial Fulfillment of the

Requirements for the Degree

of

Master of Science in Aeronautical and Astronautical Engineering

May 2019

Purdue University

West Lafayette, Indiana

THE PURDUE UNIVERSITY GRADUATE SCHOOL
STATEMENT OF THESIS APPROVAL

Dr. Carson D. Slabaugh, Chair

School of Aeronautics and Astronautics

Dr. Stephen D. Heister

School of Aeronautics and Astronautics

Dr. Robert P. Lucht

School of Mechanical Engineering

Approved by:

Dr. Weinong Chen

Head of the School of Aeronautics and Astronautics Graduate Program

[28]Do you not know? Have you not heard? The everlasting God, the LORD, the Creator of the ends of the earth, will not grow tired or weary. His understanding no one can fathom. [29]He gives strength to the weary and increases the power of the weak. [30]Even youths grow tired and weary, and young men stumble and fall; [31]but they who wait upon the LORD shall renew their strength. They will soar on wings like eagles; they will run and not grow weary, they will walk and not be faint.

- Isaiah 40

To my wife, Claire.

ACKNOWLEDGMENTS

There are several of the faculty, staff, and students of Zucrow Laboratories to whom I owe my gratitude, too many to name here. I would like to first thank my advisor, Professor Carson Slabaugh, for his guidance during my graduate studies. Thanks also belongs to Professor Robert Lucht and Professor Stephen Heister for serving on my committee. Additionally, thank you to Scott Meyer, Andrew Pratt, Aaron Lemcherfi, Rohan Gejji, Rob McGuire, Joan Jackson, and Jen Ulutas for your support throughout my time at the Maurice J. Zucrow Laboratories.

To Ian Walters, thank you for working with me throughout these studies, both in setup and execution of the experiments performed with this test article. Also, thank you for your support in developing the technical narrative surrounding this work.

Thanks also belongs to Aerojet Rocketdyne for their financial support of the presented research.

Lastly, I must acknowledge the support of my family. To my parents, Ron and Jackie Journell, thank you for your endless support and encouragement. You taught me what hard work looks like, and I will always be grateful for the opportunities you have provided me. Thank you to my sister, Whitney Journell, for being my best friend while growing up and following me to Purdue to also become an engineer (even though Biomedical Engineering is nowhere near as cool as Aerospace Engineering!) Of course, thank you to my beautiful wife, Claire, to whom this work is dedicated, for your love, support, and most of all for your patience these last couple years as I have continuously been working (or thinking about working) on research efforts and academic studies. Lastly, all my gratitude belongs to Jesus, the creator of all things. It is He who gives me strength to endure even the most difficult of times, and it is He who gives me life. *For of Him and through Him and to Him are all things. To Him be the glory forever! Amen. - Romans 11:36*

PREFACE

This document describes experimental research surrounding the application of high-speed diagnostics to a natural gas-air rotating detonation engine (RDE) at engine conditions relevant to land-based power generation. Chapter one presents the motivation behind pressure-gain combustion and the application of RDEs to gas turbines. Fundamental concepts surrounding the structure of detonation waves are presented, and the challenges inherent to an RDE are summarized. A brief literature review detailing recent research in the area of RDEs is presented, motivating the objectives of this work. A background of particle image velocimetry (PIV), particularly at high-repetition rates, is also given. Chapter two provides a detailed overview of the experimental apparatus, measurement systems, and diagnostics setup. Chapter three presents the results from a parametric survey in which operating conditions resulting in detonation behavior in the chamber were determined, results from chemiluminescence imaging of the annulus, and finally results of 100 kHz PIV measurements at the exit plane of the RDE. One contribution to scientific literature will be a direct result of the presented work, the citation/status of which is provided below. A summary of contributions from this work is presented in chapter four.

Christopher L. Journell, Ian V. Walters, Jeffrey B. Stout, Aaron Lemcherfi, Rohan M. Gejji, and Carson D. Slabaugh. High-Speed Diagnostics in a Natural Gas-Air Rotating Detonation Engine at Elevated Pressure. (manuscript in preparation for submission to Journal of Propulsion and Power)

TABLE OF CONTENTS

LIST OF TABLES

LIST OF FIGURES

Figure Page

SYMBOLS

P'	average pressure fluctuation amplitude
P_c	mean chamber pressure
u_θ	azimuthal velocity component
u_z	axial velocity component
z	axial distance from air inlet choke plane
λ	detonation cell size or cell width
θ	azimuthal location in annulus

ABBREVIATIONS

2D-FFT	two-dimensional fast Fourier transformation
APEX	agile platform for scaled engine experiments
CFVN	critical flow venturi nozzle
CJ	Chapman-Jouguet
CMOS	complementary metal-oxide-semiconductor
CTAP	capillary tube average pressure
DACS	data acquisition and control system
DMD	dynamic mode decomposition
FFT	fast Fourier transformation
LAS	laser absorption spectroscopy
Nd:YAG	neodymium-doped yttrium aluminum garnet
NI	National Instruments
PBL	pulse-burst laser
PDE	pulse detonation engine
PGC	pressure gain combustion
PIV	particle image velocimetry
PSD	power spectral density
RDE	rotating detonation engine
SSA	singular-spectrum analysis
TRL	technology readiness level
VI	virtual instrument
ZND	Zel'dovich, von Neumann, Döring

ABSTRACT

Journell, Christopher L. MSAAE, Purdue University, May 2019. High-Speed Diagnostics in a Natural Gas-Air Rotating Detonation Engine at Elevated Pressure. Major Professor: Carson D. Slabaugh.

Gas turbine engines have operated on the Brayton cycle for decades, each decade only gaining approximately one to two percent in thermal efficiency as a result of efforts to improve engine performance. Pressure-gain combustion in place of constant-pressure combustion in a Brayton cycle could provide a drastic step-change in the thermal efficiency of these devices, leading to reductions in fuel consumption and emissions production. Rotating Detonation Engines (RDEs) have been widely researched as a viable option for pressure-gain combustion. Due to the extremely high frequencies associated with operation of an RDE, the development and application of high-speed diagnostics techniques for RDEs is necessary to further understand and develop these devices.

An application of high-speed diagnostic techniques in a natural gas-air RDE at conditions relevant to land-based power generation is presented. Diagnostics included high-frequency chamber pressure measurements, chemiluminescence imaging of the annulus, and Particle Image Velocimetry (PIV) measurements at the exit plane of the RDE. Results from a case with two detonation waves rotating clockwise (aft looking forward) in the combustor annulus are presented. Detonation surface plots are created from chemiluminescence images and allow for the extraction of properties such as dominant frequency modes and wave number, speed, and direction. The chamber frequency for the case with two co-rotating waves in the chamber is found to be 3.46 kHz and corresponds to average individual wave speeds of 68% Chapman-Jouguet (CJ) velocity. Dynamic Mode Decomposition (DMD) is applied and indicates the

presence of two strong detonation waves rotating clockwise and periodically intersecting with weaker, counter-rotating waves in the annulus at certain times during operation. Singular-Spectrum Analysis (SSA) is used to isolate modes corresponding to the detonation frequency in the signals of velocity components obtained from PIV, maintaining instantaneous phase information. Axial and azimuthal components of velocity are observed to remain nearly 180° out of phase. Lastly, approximate angles for the trailing oblique shocks in the combustion chamber are calculated.

1. INTRODUCTION

1.1 Motivation

Gas turbine engines are broadly utilized, throughout the world, for air and naval propulsion as well as power generation. The mechanical and thermal design of these engines has been optimized for decades. Current research and development efforts lead to a gain in thermal efficiency of one percent every 5-10 years. It has been shown that the integration of a pressure gain combustion (PGC) technology could result in as much as seven percent gain in thermal efficiency [1]. This step-change in engine performance would have tremendous impact on fuel consumption and carbon dioxide emission production from combustion devices.

Detonation waves, which are shock-coupled reactions fronts, combust the fuel-oxidizer mixture at locally-elevated pressures [2]. The shock wave associated with the supersonic reaction front provides a sharp increase in pressure and temperature immediately before the reaction takes place, thus allowing for a higher pressure benefit for the same heat release [2, 3]. Figure 1.1 provides a comparison between an ideal Humphrey (detonation) cycle and the Brayton cycle on a pressure-specific volume ($P - v$) diagram. Here, the Brayton cycle is shown with an operating pressure ratio (OPR) of ten and the detonation cycle is shown with an OPR of two. It is seen that even with 80% lower OPR, the detonation cycle still produces additional work compared to the Brayton cycle, indicated by the shaded gray region.

Figure 1.2 presents another comparison between a detonation cycle and a Brayton cycle on an enthalpy-entropy ($h - s$) diagram. Here, these cycles have been limited to the same maximum cycle temperature. In the detonation cycle, isentropic compression (1 to 2) is followed by further, non-isentropic compression (2 to 2_s) associated with the leading shock wave in a detonation, thus bringing the cycle to a higher

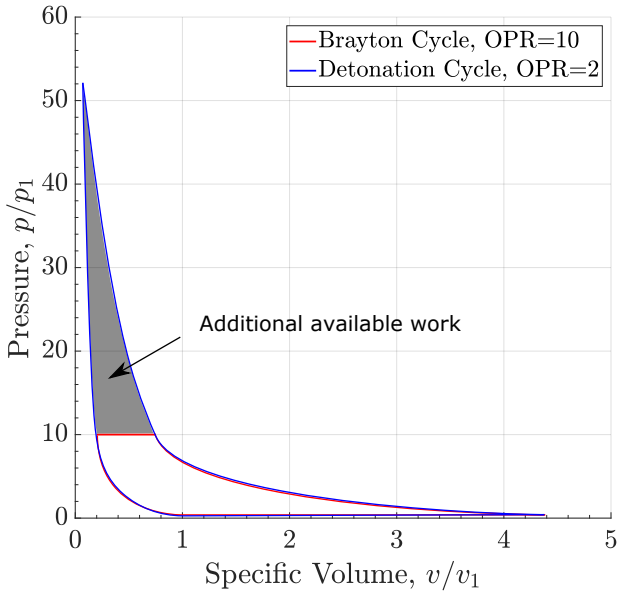

Fig. 1.1. $P-v$ diagram comparing Humphrey (detonation) cycle with OPR = 2 to Brayton cycle with OPR = 10.

pressure than in the Brayton cycle. Then, because the reaction time-scales are much shorter than those of gas expansion, heat addition takes place along an isochor instead of an isobar, again providing an additional pressure-boost to the cycle. Because of these higher pressures and heat addition along an isobar, the total entropy production to produce the same maximum cycle temperature is much less in the detonation cycle. Thus, as seen in Fig. 1.2, the heat extracted isentropically for work output is much higher for the detonation cycle than for the Brayton cycle. This further illustrates that an ideal detonation cycle produces a higher pressure benefit for the same heat release than an ideal Brayton cycle.

Pulse Detonation Engines (PDEs) have been investigated as a means to achieve PGC in practical devices via detonations [4,5]. The operation of a PDE (illustrated in Fig. 1.3a) involves the cyclic process of filling a combustion chamber with a reactant mixture, ignition of the mixture (initially as a deflagration), the subsequent transition of the combustion wave from a deflagration to detonation (DDT), then (finally) a

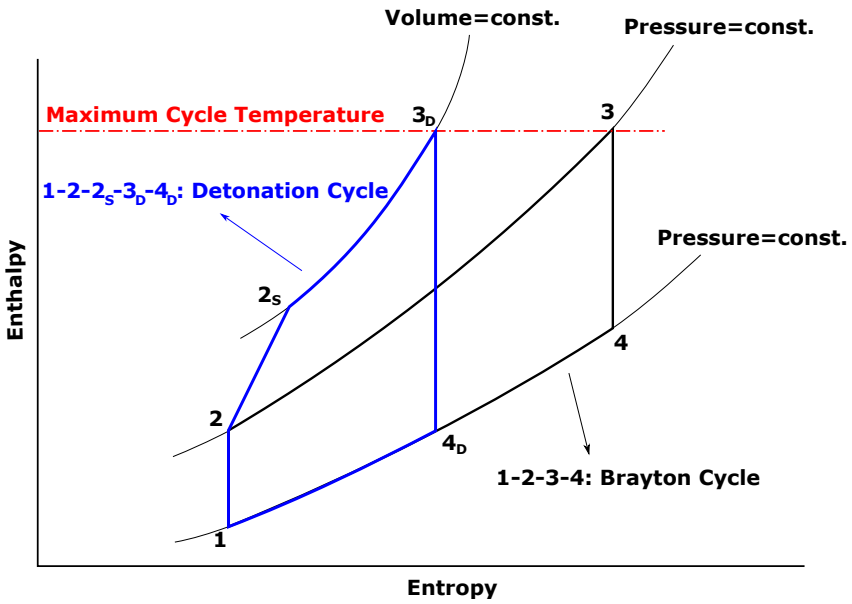

Fig. 1.2. $h - s$ diagram comparing detonation cycle to Brayton cycle.

chamber purge before the cycle repeats. The PDE cycle is difficult to implement because of the mechanical and hydrodynamic challenges to achieve all of these steps quickly, and, hence, the operating frequency of a PDE is limited to only 100-200 Hz [3].

Rotating Detonation Engines (RDEs) have also been investigated as a means to realize PGC in practical devices via detonations [6,7]. In an RDE, a detonation wave circumscribes (or rotates) around the annular combustion chamber at frequencies on the order of 1-10 kHz [3], illustrated in Fig. 1.3b. Due to the high-speed detonation wave (or waves, as a wave can divide into two or more) being sustained, ignition is required only once and a dynamic injection process is achieved completely with the hydrodynamic response of the injector, thus no mechanical valves are needed as in the case of a PDE. This makes the RDE a strong candidate for a viable PGC technology.

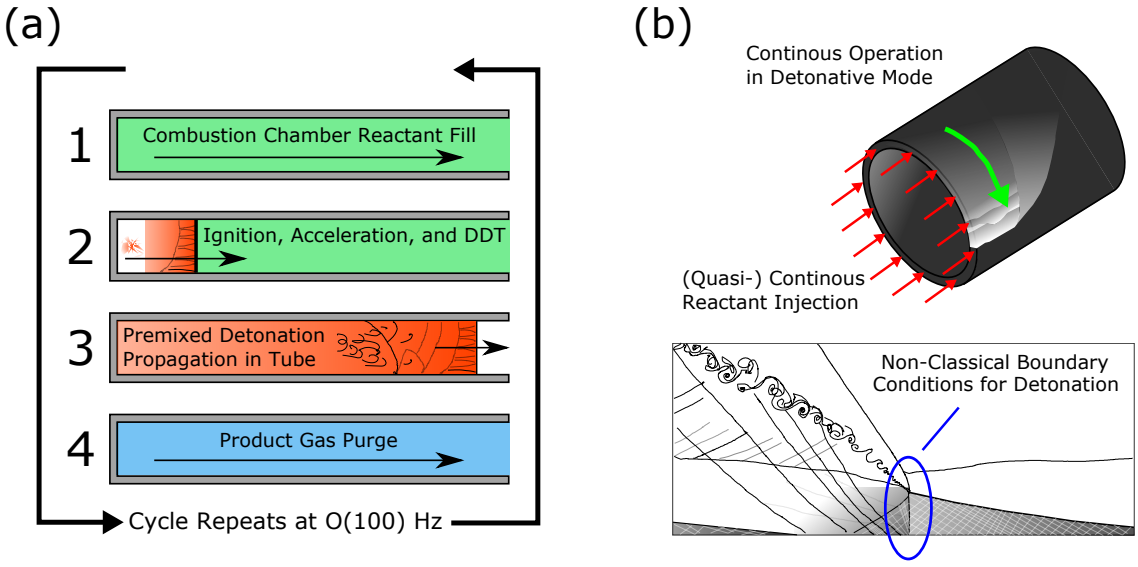

Fig. 1.3. PDE operating cycle (a) compared to RDE operating cycle (b).

1.2 Detonation Wave Structure

As previously defined, detonations are shock-coupled reaction fronts that travel at supersonic speeds. The Chapman-Jouguet (CJ) theory and the Zel'dovich, von Neumann, Döring (ZND) model of the detonation structure were developed assuming steady and one-dimensional flow. Previous experimental studies of detonation physics under classical conditions saw close agreement between steady, one-dimensional theory and the results, despite the fact that detonation wave structure is inherently unsteady and three-dimensional in nature. Figure 1.4 presents a schematic from Lee and Radulescu [8] that illustrates the idealized structure of a traveling detonation front. A detonation front consists of an incident shock immediately followed by a chemical induction layer. As products soon begin to expand after the detonation passes, a shear layer (or slip line) forms, along with a Mach stem. Transverse shocks also trail behind a detonation front. These three shock features (incident shock, Mach stem, transverse shock) intersect to form an area with extremely high local pressures, and thus points with high energy densities. These areas are termed triple

points. Triple points move in time as a detonation front propagates and triple point trajectories form cells. A cell size or cell width, λ is the maximum transverse distance between triple point trajectories and is a frequently referenced parameter in detonation literature and an important design parameter for the selection of an RDE combustor annular gap width.

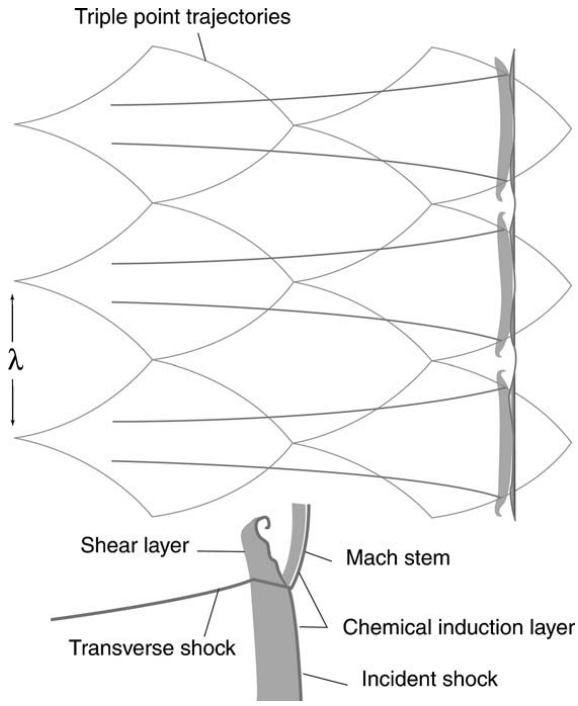

Fig. 1.4. Schematic from Lee and Radulescu illustrating idealized structure associated with a detonation front including transverse shocks, Mach stem, and triple point trajectories [8].

As triple points are locations of maximum heat release (maximum pressure gain), they are an important feature to consider when designing pressure-gain combustion devices such as an RDE. Radulescu and Lee performed studies on the effect of porous boundary conditions to the stability of a propagating detonation wave [9]. Figure 1.5 shows open-shutter photographs of detonations propagating through a stoichiometric mixture of acetylene (C_2H_2) and oxygen. Here, the walls change from solid boundaries to porous boundaries in the length of the channel, and the effects of lowering initial

pressure are observed. It is seen that for all cases, the effect of porosity in the walls causes relief in the reflecting transverse shock waves, and cell sizes increase in time until finally the detonation front fails to continue for low enough initial pressure (Fig. 1.5c). This basic fact of detonations is likely one cause of deficits in velocity and pressure relative to CJ values observed in RDEs, as the injection boundaries have a lower acoustic impedance associated with them than a solid boundary and there is axial relief in the aft end of the combustion annulus.

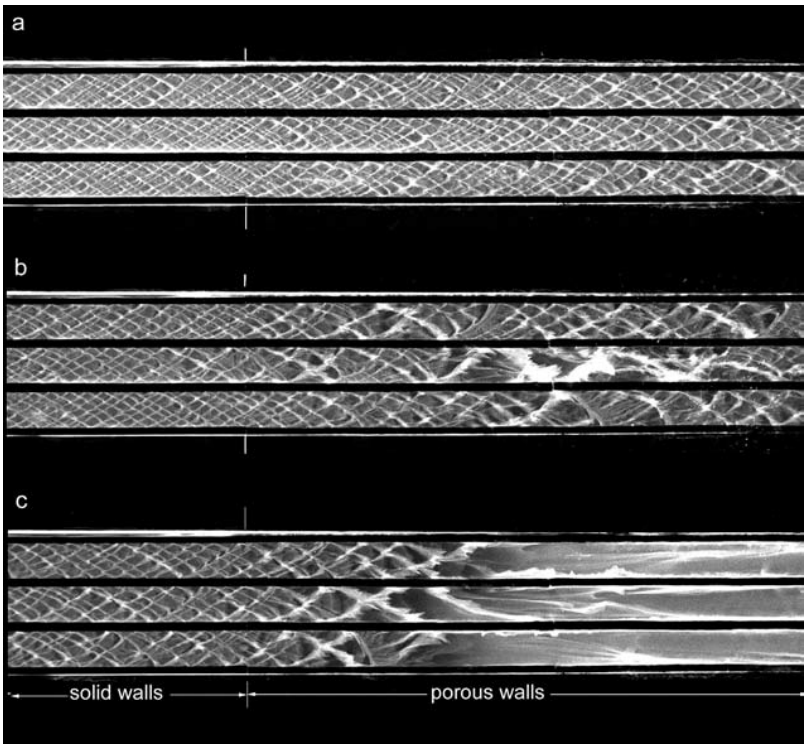

Fig. 1.5. Open-shutter photographs of a detonation propagating from a solid walled section to a section with porous walls through a stoichiometric C_2H_2-O_2 mixture at initial pressures of (a) 3.6 kPa, (b) 3.2 kPa, and (c) 2.7 kPa [9].

In addition to porosity and low initial pressures causing large cell sizes, certain reactant combinations lead to various cell sizes as well. Walters *et al.* recently provided a comparison between the detonation cell sizes for various fuel/oxidizer combinations, shown in Fig. 1.6. It is immediately apparent that increasing the initial pressure

and temperature both decrease the average cell width following a detonation. The correlations in Fig. 1.6a also show that mixtures containing air instead of pure oxygen result in larger cell widths. This is attributed to the lower energy density of the mixture, as air contains 76.8% inert nitrogen by mass, and thus cells must be larger to have the same heat-release necessary to sustain a detonation front. Further, Walters *et al.* presents a correlation of known data that shows the effect of using methane-air instead of hydrogen-air mixtures increases the necessary cell size by an order of magnitude or more, depending on initial conditions. Thus, increased cell size for natural gas-air propellants requires that the chamber width of an RDE be larger than an RDE operating on hydrogen-air or hydrogen-oxygen to accommodate enough cell-widths to sustain a detonation in the chamber. To design and operate a natural-gas RDE of feasible scale, these trends indicate operation with an initial pressure of at least 10 atm to be in a range of cell sizes roughly between 10 and 30 mm.

Although RDEs have certain operational advantages, there are inherent challenges as well. The boundary conditions found in an RDE deviate tremendously from the classical boundary conditions associated with detonations. RDEs do not present the classical boundary conditions, acoustic or otherwise, that were assumed in the development of CJ theory and the ZND model of detonations, and deficits in wave properties are observed. These deficits are ascribed to the deviations from classical boundary conditions, outlined in Fig. 1.7. Deviations in boundary conditions include variation in aspect ratio and curvature, acoustic wall impedance of the injector(s), compressible turbulence and contact surface dynamics, and mixture fraction stratification. All of these boundary conditions together produce the complex rotating detonation wave structure in an RDE as illustrated in the left half of Fig. 1.7. More research on detonation wave structure in RDEs and understanding the effects of various boundary conditions and operating parameters is necessary to advance RDE technology to a technology readiness level (TRL) sufficient for the application to practical devices.

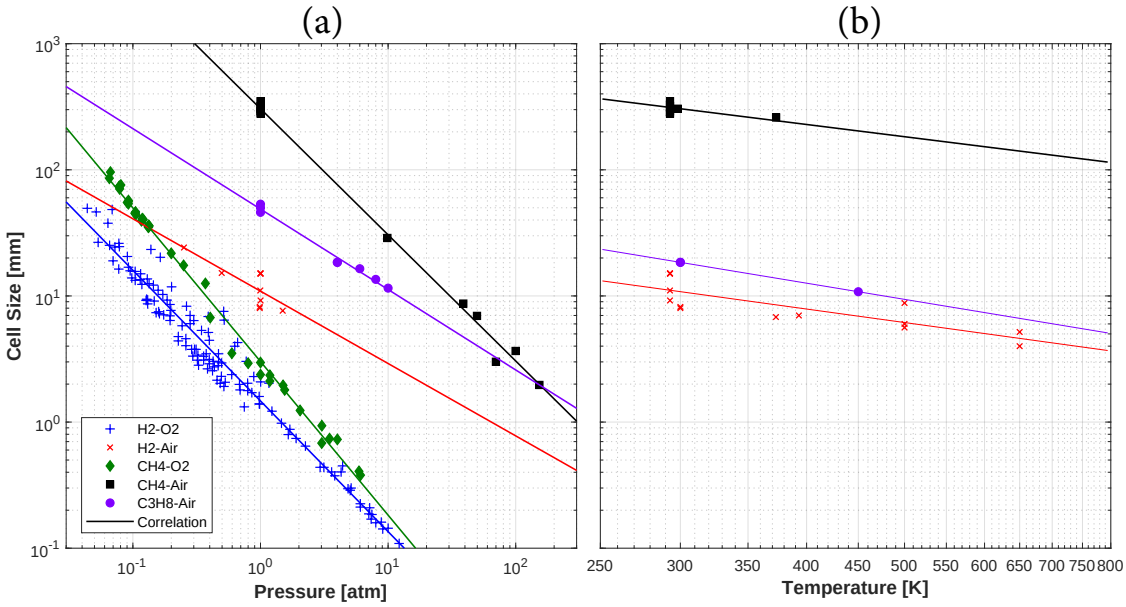

Fig. 1.6. Cell size data for detonations compiled by Walters *et al.* showing effects of initial pressure (a) and temperature (b) on detonation cell size [10]. Data was compiled from the Graduate Aerospace Laboratories of the California Institute of Technology (GALCIT) detonation database [11], Stevens *et al.* [12], Bauer *et al.* [13], and Siwiec and Wolański [14].

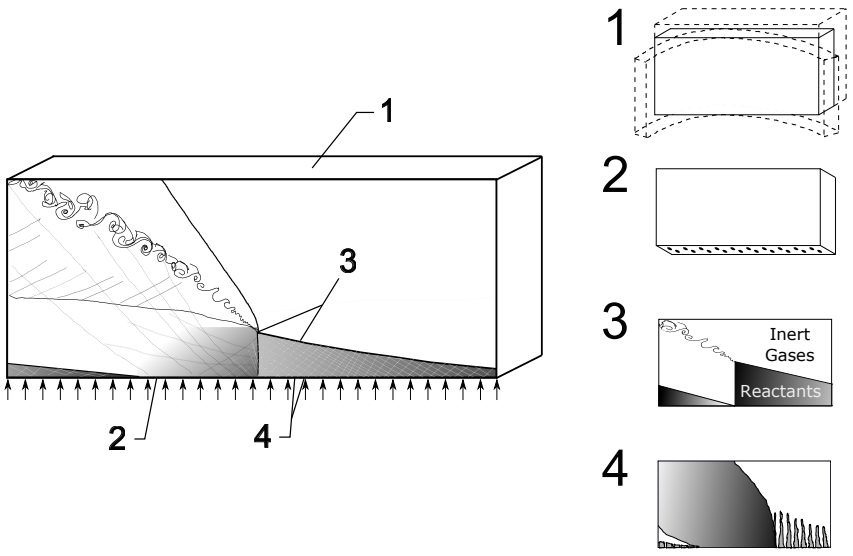

Fig. 1.7. Unwrapped view of RDE showing non-classical boundary conditions: (1) Aspect ratio and curvature. (2) Acoustic wall impedance of injector. (3) Compressible turbulence and contact surface dynamics. (4) Mixture fraction stratification.

1.3 Current State of RDE Research

Early research of RDEs began in the late 1950s and early 1960s. Voitsekhovskii is credited with the first experimental study and demonstration of continuous detonation combustion [15, 16]. This study was motivated by the spinning detonation phenomenon (outlined in detail by Lee [17]) and sought to achieve a steady (or continuous) spin detonation to provide another means for experimental observation of detonation physics. For these studies, premixed acetylene-oxygen propellants were used. Inspired by the work of Voitsekhovskii, Nicholls *et al.* performed studies on the feasibility of a rotating detonation wave rocket combustor with an annular chamber [18]. Many challenges were experienced and no other studies on RDEs took place in the United States for several decades following this work. Though detonation was achieved, no waves were sustained. Nonetheless, the overall architecture presented by Nicholls *et al.* closely resembles that of RDEs presented in the literature today.

The experimental work in 1975 of Bykovskii *et al.* was the first representation of a sustained continuous spin detonation within an RDE [19]. In this work, photographs were obtained of methane-oxygen and acetylene-oxygen detonations in a long annular combustion chamber. Since this work, Bykovskii has been a leader in the development of RDEs. A review of many of these early RDE studies is provided by Bykovskii [6]. Bykovskii *et al.* most recently published results from a study detailing the scaling parameters in an RDE operating on syngas-air mixtures [20]. This work presents the parameter of fill height within an RDE chamber and the importance it carries when designing an RDE for various operating conditions.

Applications of RDEs to various aerospace propulsion systems such as turbojets, high-speed air-breathing devices, and rockets have been investigated. Most research for air-breathing devices has used hydrogen fuel [21–26]. Fewer efforts have been made to investigate propellant combinations relevant to the application of an RDE to land-based power generation, particularly natural gas and air. Depperschmidt *et al.* presented experimental results from an oxygen-enriched methane-air RDE operating

at near-stoichiometric conditions [27]. In these experiments, the outer diameter for the combustor annulus was only 10 cm with an annular gap of 1 cm, and air mass flow rates did not exceed 0.152 kg/s. The tested RDE design was developed by Aerojet Rocketdyne to be modular by nature. To provide similar back pressures as in the case of a turbine downstream of the RDE combustor, a converging-diverging choke plate was installed at the exit of the combustor annulus. Results showed successful operation in a single-wave mode.

Walters *et al.* has investigated the operation of an oxygen-enriched natural gas-air RDE at elevated pressures using high-frequency pressure measurements and direct, high-speed imaging of the combustor annulus [10, 28]. The outer diameter for the combustor annulus was 22.8 cm for those experiments, and total mass flux values approached 300 kg/s.m^2 in several cases. However, only counter-rotating detonative modes were observed. Therefore, there is still a need to further investigate and characterize RDE operation with natural gas-air propellants at elevated pressures and temperatures relevant to land-based power generation applications.

Present RDE research has mainly relied on the acquisition and analysis of high-frequency pressure measurements and/or ion probe data, as well as high-speed imaging [22, 23, 29, 30]. These measurements allow for approximations of average wave frequency and speed to be made. Bennewitz *et al.* presented a method for extracting instantaneous mode characteristics from direct high-speed imaging of the combustor annulus, allowing for more quantitative conclusions to be made based on these types of images [31]. The method is outlined in Fig. 1.8 and is briefly summarized here. First, raw images were divided into intervals of 1,000 frames each such that in any given interval, the images moved relatively little. For each interval, an average background subtraction was applied to increase contrast between the detonation wave(s) and the image background. One average image was calculated for each interval and subtracted from each image within that interval. A correction factor is defined as

$$\beta_n = \frac{\Sigma_{x,y}\bar{p}_k(x,y)}{\Sigma_{x,y}p_k(x,y,n)} \tag{1.1}$$

and is applied to each image before subtracting the average image. Here, $p_k(x, y, n)$ is a three-dimensional matrix of pixel intensity data where x and y give the column and row, respectively, of each pixel and n the image number within the k^{th} interval. $\bar{p}_k(x, y)$ is the average image for the k^{th} interval. Multiplying each image by the correction factor β_n and subtracting the average image from each individual image within an interval gives

$$p_{k,corr.}(x, y, n) = \beta_n p_k(x, y, n) - \bar{p}_k(x, y) \tag{1.2}$$

where $p_{k,corr.}$ is also a three-dimensional matrix of pixel intensity data, both corrected and average-background subtracted, as a function of both time and location. These image pre-processing steps are shown in the top half of Fig. 1.8.

To locate the annulus in each image, Bennewitz *et al.* first defined a Cartesian mesh, with square cells arranged in a 50 x 50 grid. An integrated (summed) pixel intensity was determined for each cell for all images, and a Fourier transform analysis was performed for all 2,500 cells in all 1,000 images for each interval. As the detonation frequencies for this work were observed to be bounded between 20-50 kHz, the amplitudes corresponding to this frequency range were summed for each cell in each image and the top 100 cells were used along with a Taubin fit [32] to locate the annulus. Finally, a polar mesh is defined with one radial bin and 200 azimuthal bins, and an integrated (summed) pixel intensity for each bin in each image in each interval is determined. This provides spatially and temporally resolved information of pixel intensity in the RDE annulus, which can be presented on what is termed a detonation surface as intensity plotted over azimuthal location vs. time. Bennewitz presents subsequent methods to further analyze a detonation surface to obtain quantitative characteristics surrounding the operation of an RDE, including wave number, operating frequency, wave speed, etc. This technique was applied, along with thrust measurements, to make performance characterizations of a methane-oxygen RDE for various mass flow rates not exceeding 0.5 kg/s, equivalence ratios, and injector configurations. Throughout these tests, operation modes observed included wave numbers

ranging from 2-14 with wave speeds ranging from 33-71% CJ velocity for each respective case.

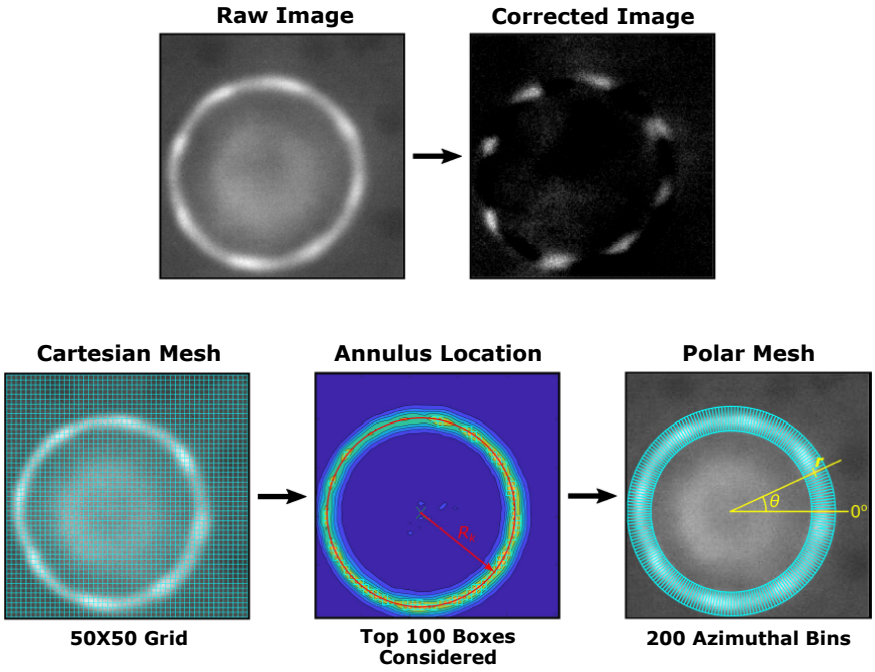

Fig. 1.8. Image correction steps (top) and post-processing steps (bottom) to create a detonation surface as presented by Bennewitz *et al.* [31].

Thrust measurements during RDE operation have been performed to assist in the determination of performance characteristics [24, 31, 33]. Species-specific chemiluminescence has also been applied to RDEs. Rankin *et al.* performed 20 kHz OH* chemiluminescence imaging of a hydrogen-air RDE through a quartz outer-body to determine wave structure and average wave frequencies/speeds for various conditions [21]. Few studies present results of measurements at the RDE exit plane where information such as emissions, flow velocities, trailing shock structures, and more could possibly be obtained. At the exit plane, physical probes would disturb the flow, so non-intrusive diagnostic techniques should be applied. 30 kHz OH* chemiluminescence imaging was performed by Tobias *et al.* in the exit plume of an RDE to show the existence of reaction zones downstream of the combustor [34]. Researchers

have also applied laser absorption spectroscopy (LAS) techniques to the exit planes of RDEs to collect measurements of temperature, H_2O concentration, and axial exit velocity (at a point) [35,36]. There remains a significant need for measurements at the exit plane of an RDE, particularly for propellant combinations relevant to land-based power generation.

1.4 Particle Image Velocimetry

Flow visualization techniques have been applied for centuries. After the onset of photographic recording techniques in the late 19th century, qualitative flow visualization results could be shared within the scientific community. Pioneering scientists such as Ludwig Mach and Ludwig Prandtl applied qualitative flow visualization techniques such as smoke to visualize streamlines in air or iron ore particles on the surface of water to track flow around a test article suspended at the water's surface [37, 38]. The past century has seen tremendous advancements in laser technologies, digital recording techniques, and computers which have allowed this basic idea behind qualitative flow visualization to grow into a means to obtain quantitative measurements of velocity within complex flow fields.

One such measurement is particle image velocimetry (PIV), a quantitative, non-intrusive imaging technique that uses a laser sheet to track seed particles introduced to the flow, providing two components of velocity within the laser sheet plane [39, 40]. Though there are various forms of PIV, only one will be discussed here. Figure 1.9 shows an example of an experimental application of two-component, two-dimensional (planar) PIV to flow in a wind tunnel. The wind tunnel flow is seeded with tracer particles at a medium seeding density appropriate for PIV [39]. A pulsed laser is formed into a sheet and illuminates the particles at two separate, closely spaced instances in time while a high-speed camera captures images during the brief moments of illumination. In this double-frame/single-exposure setup, two images (an image pair) are obtained. The images are calibrated to obtain appropriate scale and any

necessary pre-processing steps, such as average background subtraction to maximize contrast between particles and the image background, are applied.

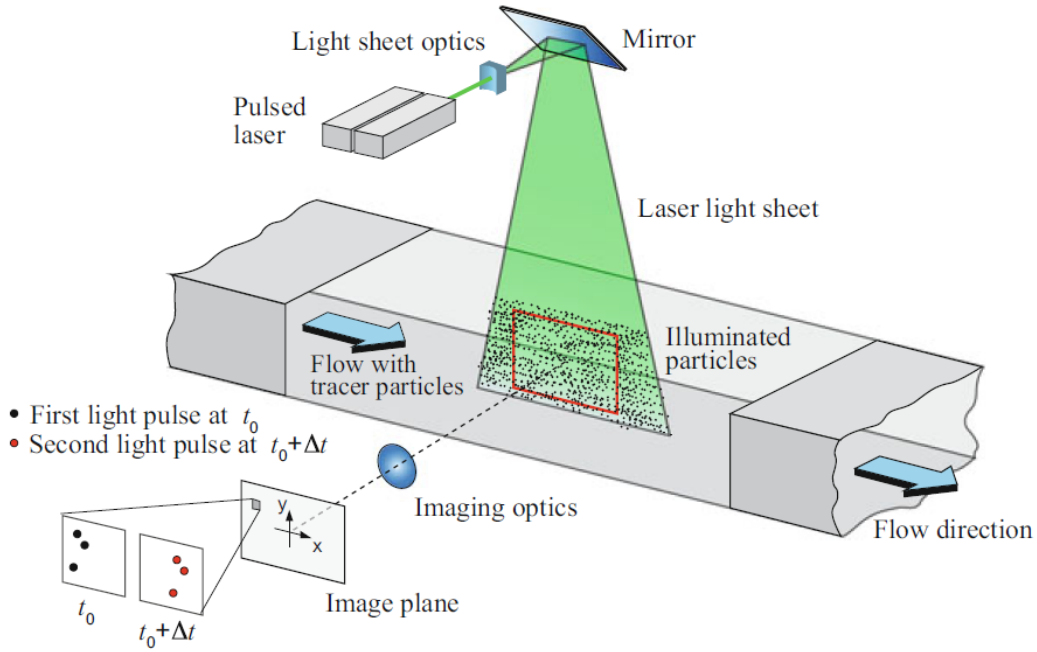

Fig. 1.9. Example schematic of experimental setup for planar two-component PIV in which double-frame/single-exposure imaging is applied [39].

Once calibration and any pre-processing of the images is complete, the images are then processed through a cross-correlation method, outlined in Fig. 1.10. Each image is divided into small areas that are referred to as interrogation windows, and cross-correlations are calculated between the images for each interrogation window. Statistical methods are applied to generate a correlation plane with peaks corresponding to possible solutions of average particle displacement within a particular interrogation window. The highest peak within this correlation plane gives the most likely displacement (dx, dy) of the ensemble of particles within the interrogation window. Once all interrogation windows are analyzed and proper correlations are found, a two-dimensional vector field with two-components of velocity is obtained.

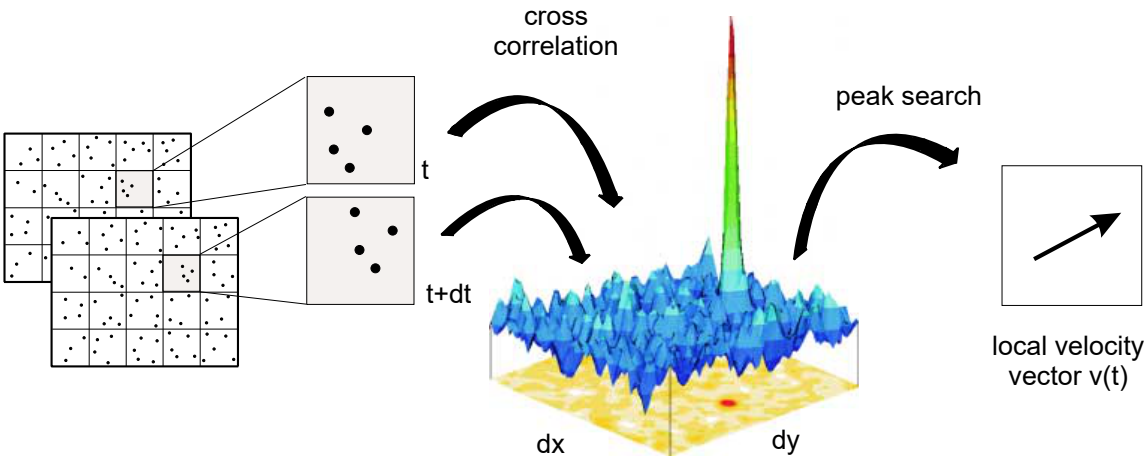

Fig. 1.10. Cross-correlation for two-component, two-dimensional PIV with double-frame/single-exposure imaging [41].

Recent advancements in pulse-burst laser technology and high-speed cameras have allowed for ultra-high repetition rate (100 kHz and above) laser diagnostics for various measurements in high-speed flows [42]. Wernet and Opalski were pioneers in developing and applying a time-resolved PIV system that utilized a pulse-burst laser, demonstrating the system at a repetition rate of 1 MHz and obtaining measurements in supersonic jet flows at rates up to 25 kHz [43, 44]. Higher PIV measurement rates of up to 1 MHz have been obtained by trading resolution and/or quantity of measurements in a vector set [45, 46]. Several researchers have successfully made 100 kHz PIV measurements sufficient for obtaining relevant spatiotemporal spectral information in various turbulent and/or supersonic flows [47–49].

Recently, Depperschmidt *et al.* performed 50 kHz, time-resolved PIV at the exit of an oxygen-enriched, methane-air 10 cm RDE [27]. As previously stated, this RDE operated at near-stoichiometric conditions and low values of total mass flux. A converging-diverging choke plate was installed at the exit of the RDE combustion annulus, and PIV measurements were performed immediately downstream of the RDE exit plane, as illustrated in the schematic shown in Fig. 1.11. A seeder was used to

introduce small particles (200 nm zirconium-dioxide, ZrO_2) to the main air flow. A separate source of air was used for the seeder and was independently regulated to control the percentage of seeded air in total air flow to the RDE, and thus seed densities for imaging. For the cases presented, a Photonics DSH-532-35 laser system was used to provide laser pulses and a Photron SA-5 high-speed camera obtained images at a resolution of 256 x 232 pixels. This resolution and the camera location gave a spatial resolution of 95.24 μm/pixel, imaging a 24.38 mm x 22.10 mm plane, shown in Fig. 1.11. A combination of spherical and cylindrical lenses were applied to form a laser sheet of appropriate height and thickness in the measurement plane. Vector fields for the entire region were obtained, however only vectors at four points near the center of the measurement plane and closest axially to the engine exit where radial velocity component could be assumed zero were considered. For each test, 1,030 image pairs were obtained, yielding 20.6 ms of PIV data. PIV acquisition began immediately following the initiation of a detonation wave in the chamber, so measurements were not immediately of steady state operation but rather engine startup.

PIV was performed for a case with higher total mass flow rate which produced a single-wave mode propagating in the clockwise direction. Velocity vectors were filtered out if axial velocity component was not between 25 m/s and 3,000 m/s or if circumferential velocity component magnitude was greater than 2,000 m/s. Measured axial velocities varied tremendously in this case, ranging from 250 m/s to 1,500 m/s. Circumferential velocities were measured to fluctuate periodically with the passing of a detonation wave from -250 m/s to 750 m/s, corresponding to flow in the opposite direction of the propagation of the detonation wave (counterclockwise) and the same direction as the propagation of the detonation wave (clockwise), respectively. This case yielded many unresolved vectors in the four locations of interest tangent to the RDE center-body at the exit plane. This was attributed to flow unsteadiness during startup and seed densities decreasing as increasing chamber pressure back-pressured the seeder flow, preventing it from combining with the main oxidizer flow.

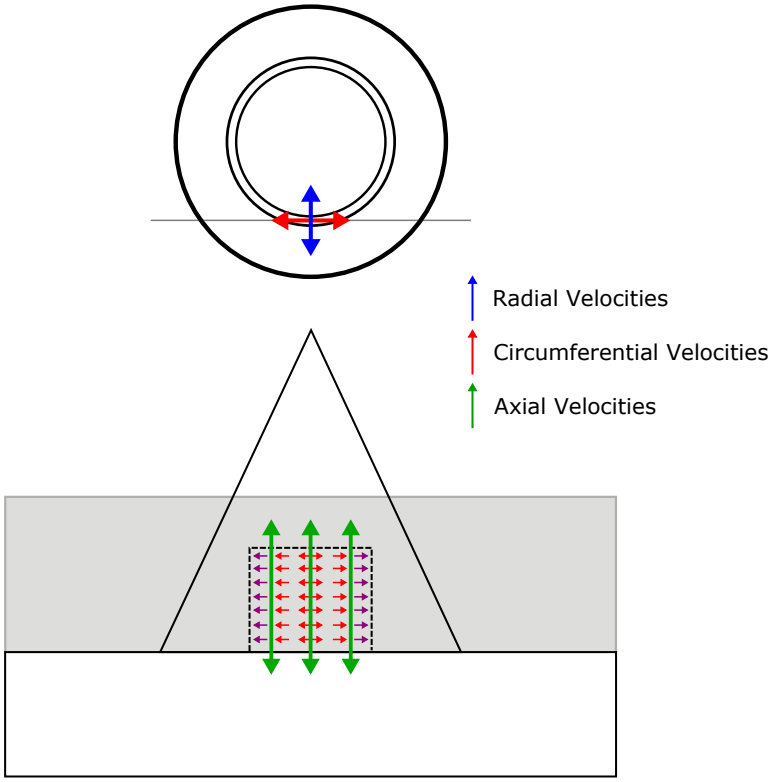

Fig. 1.11. Front view (top) and bottom view (bottom) showing measurement plane relative to RDE. Also shown is an illustration of velocity components of interest. Radial velocity component (shown in blue) is assumed to be zero at points tangent to the RDE center-body [27].

In an attempt to achieve better measurements, PIV was performed at a lower mass flow rate. It should be noted that this case used high amounts of oxygen to obtain a single wave propagating counterclockwise in the chamber. Velocity fields obtained during this test are shown in Fig. 1.12. Periodic nature was observed, however there were frequent time slices with little to no calculated velocity vectors. Seed densities were determined to be sufficient for these images, and the lack of resolved vectors was attributed to increasing differences in laser power between pulses as the test progressed, leading to image pairs with differing overall intensities. Despite these challenges and loss of vector fields later in the test, some trends were observed from the resulting vector fields shown in Fig. 1.12. The first vector field shown was

calculated from an image pair taken shortly after the passing of the detonation wave in the chamber, and flow velocity magnitudes are at their highest with flow primarily in the axial direction. Throughout the first four images in the sequence, flow is observed to turn in the direction opposite to the propagating detonation wave. The trailing oblique shock wave starts to appear in the measurement plane again in the the first image in the second row, turning the flow to follow in the same circumferential direction as that which the wave is traveling. Though not shown, it is assumed the velocity vectors quickly turn to axial flow after the detonation passes through the measurement plane, and the cycle would repeat. These measurements provide some insight in the exit flow of an RDE, but the need for higher-quality measurements of velocity in the exit plane with more, time-resolved data still exists.

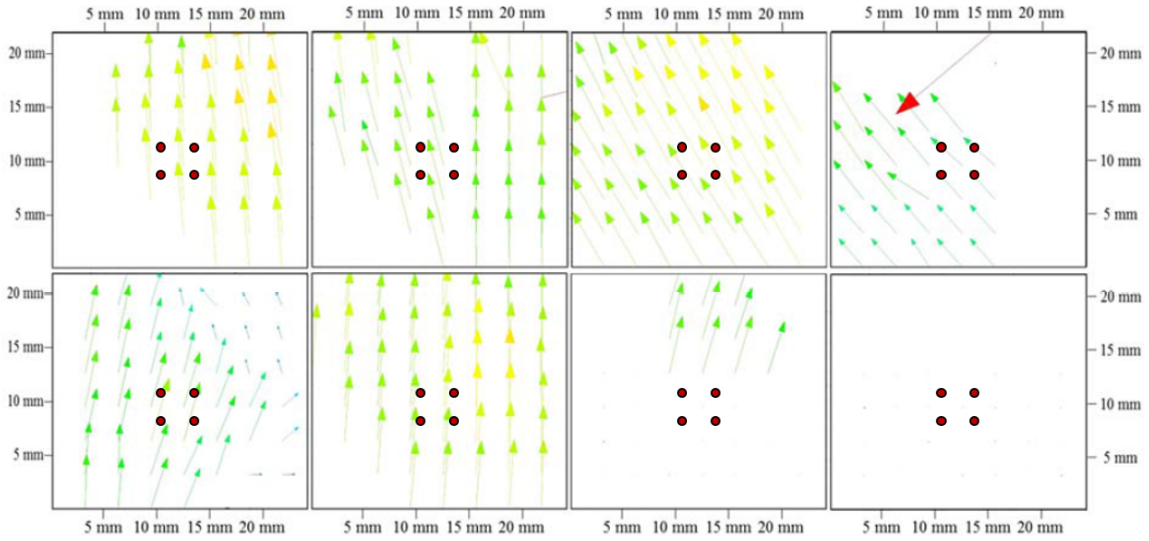

Fig. 1.12. Calculated vector fields for one period associated with passing of a detonation wave in the lower mass flow case. Progression in time moves left to right, top to bottom [27].

1.5 Objectives

The present study details an experimental investigation of a 23.9 cm diameter RDE designed to operate with natural gas and air as propellants with oxygen enrichment of the oxidizer flow. First, a parametric survey of detonation behavior in the combustor was performed and combustion performance was quantified. An array of high-frequency pressure transducers was used to collect pressure measurements to determine chamber frequencies and pressure fluctuations with the passing of a detonation wave. Once highest performing cases were determined, 44 kHz direct chemiluminescence imaging of the annulus was performed and images were analyzed via a detonation surface and two-dimensional fast-Fourier transform as well as dynamic mode decomposition. This allowed for the determination of spectral content withing the chamber and the isolation of various spatial modes within the chamber that describe wave motion. Finally, 100 kHz time-resolved PIV measurements at test conditions of relevance to the land-based power generation industry are used to further characterize the performance of the combustor. Singular-spectrum analysis is applied to show the relation between two components of velocity.

2. EXPERIMENT DESCRIPTION

2.1 Maurice J. Zucrow Laboratories and Facilities

Purdue University's Maurice J. Zucrow Laboratories has a long history of contributions in experimental research of both gas turbine and rocket propulsion systems at operating conditions relevant to the propulsion and power-generation communities [50, 51]. Zucrow has expanded tremendously in both size and capabilities since the establishment of the laboratories in 1948. Most recently, a new high pressure combustion laboratory with four 500 sq. ft. test cells, one 1,000 sq. ft. test cell, a temperature/humidity controlled 2,000 sq. ft. laser laboratory, and a natural gas fired high pressure air heater was constructed [52]. The present experimental studies were performed in one of these 500 sq. ft. test cells and utilized the laser laboratory and the high pressure air heater. Facility capabilities of the high pressure combustion laboratory are described in detail by Meyer *et al.* [52] and only details relevant to the experimental studies in the present work are summarized here.

The aforementioned air heater is capable of providing air at 55 bar and 1090 K at a flow rate of 4.0 kg/s. Air is supplied from an on-site air compressor plant at 0.45 kg/s at 150 bar and is stored in compressed gas storage vessels closely coupled to the air heater. The storage vessels hold a volume of 9,000 kg of clean, dry air at the maximum pressure of 150 bar and can provide upwards of 23 kg/s blow-down mass flow rates.

A bulk supply skid compresses natural gas to a maximum pressure of 250 bar before supplying the fuel to the test cells and experiments. Gaseous oxygen from gas cylinders is supplied through dedicated flow lines at mass flow rates up to 0.91 kg/s and pressures up to 180 bar. Liquid nitrogen is stored onsite and pumped to 400 bar for use in several experiments. Boil off from the liquid nitrogen supply is also

pumped to 400 bar and over 9,000 kg of gaseous nitrogen is stored at this pressure for pneumatic controls and purges. A facility water softener is used to provide softened water at the municipal supply pressure (6-7 bar) to experiments for cooling purposes.

Each test cell in the new high pressure combustion laboratory has its own dedicated data acquisition and control system (DACS). A National Instruments (NI) LabVIEW Virtual Instrument (VI) is used to control valves and regulators as well as monitor conditions in fluid supplies, lines, and test articles. The VI has auto-sequence control capabilities and has a live red line monitoring system that can be used for aborts. A separate DACS and VI is used to control shared fluid system supplies including those for air and natural gas. Pressure transducers and thermocouples are sampled at 1,000 Hz. A separate, high-frequency DACS is used to collect high-frequency measurements at rates up to 1 MHz.

2.2 Agile Platform for scaled Engine eXperiments

Experiments in the present study were performed on the Agile Platform for scaled Engine eXperiments (APEX) in one of the aforementioned 500 sq. ft. test cells in Zucrow Laboratories new high pressure combustion laboratory. The test platform, shown in Fig. 2.1, has a 44.5 kN single component thrust measurement stand and a wide array of propellants feed systems. Fluid services for the test platform were sized to provide up to 10 kg/s of non-vitiated, heated air and temperatures at the test article of up to 810 K (590 K if flowing 10 kg/s). The platform also provides up to 1.8 kg/s of natural gas and 2.3 kg/s of gaseous oxygen.

Propellant mass flow rates were controlled and metered using critical flow venturi nozzles (CFVNs) that comply with ISO specifications [53]. Pressure ratios across the CFVNs were controlled such that the nozzle remained choked through the entire duration of each test, thus isolating the propellant supplies from the dynamic combustion processes in the chamber and providing constant mass flow rates. Pressure and temperature measurements were collected upstream of each CFVN to allow the

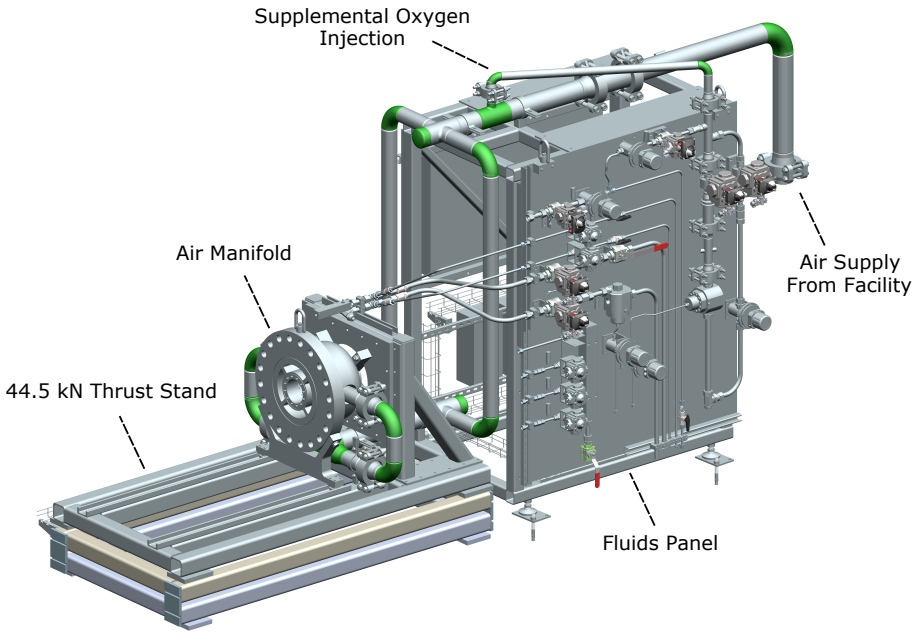

Fig. 2.1. A rendering of the APEX test stand showing key features.

computation of propellant mass flow rates. Propellants were treated as real gases for the mass flow rate computations, as well as for the computation of acoustic velocities and other thermodynamic data, by using The NIST Reference Fluid Thermodynamic and Transport Properties Database (REFPROP) to compute all fluid thermophysical properties [54]. For calculations involving natural gas, the fluid was treated as a mixture based on a monthly average of mole fraction of major species reported by the distributor (CH_4 92.4%, C_2H_6 6%, N_2 1%, CO_2 0.3%, C_3H_8 0.3%).

For each test, ignition was achieved via a pre-detonation device with hydrogen and oxygen as propellants. Hydrogen and oxygen for the pre-detonation device were supplied from regulated gaseous bottles closely-coupled to the stand. Prior to ignition, propellant run-valves were opened and allowed sufficient time to fully prime the chamber. Propellant run-valves were closed and nitrogen purges were established to terminate combustion in the main chamber. The steady-state test duration was limited between 0.5 and 1.5 seconds, depending on the specific test conditions, as no

methods of active cooling were applied to combat the high thermal power densities associated with detonative combustion.

2.3 Aerojet Rocketdyne 23.9 cm RDE

Figure 2.2 shows a schematic of the RDE combustor that was used in the present study. The RDE annular combustion chamber has an outer diameter of 23.9 cm with a 15.2 mm channel width. Air (along with any supplemental gaseous oxygen) flows through an annulus around the RDE center-body and is choked before entering the main combustion chamber to isolate the air manifold from chamber dynamics. Natural gas is then injected immediately downstream of the main air choke plane, as indicated by the red arrows in Fig. 2.2. This RDE was capable of reaching chamber pressures of 2 MPa and air inlet temperatures exceeding 700 K.

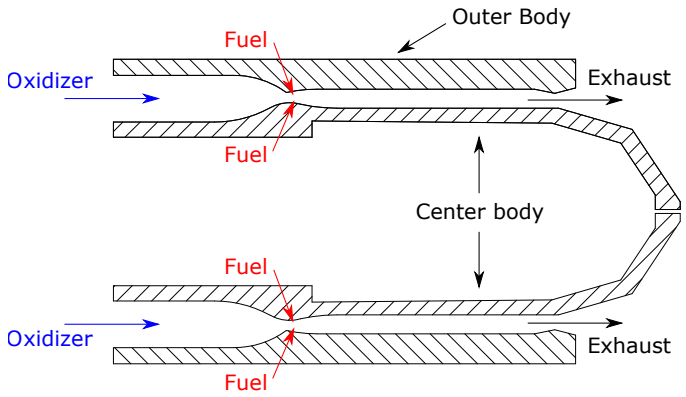

Fig. 2.2. Schematic of the RDE combustor.

2.4 Instrumentation and Diagnostics

The combustor was instrumented with integral and time-resolved pressure measurements at multiple locations. GE Sensing UNIK 50E6 transducers were used for integral measurements at 1 kHz for condition monitoring as capillary tube average pressure (CTAP) measurement of the mean chamber pressure. High frequency (1

MHz sampling rate) pressure was measured using piezoelectric PCB transducers installed at two axially distributed locations in the combustion chamber. Figure 2.3 and Table 2.1 together specify instrument port locations in the propellant manifolds and combustion chamber. The axial coordinate z is based on the distance from the air inlet choke plane to the downstream port location.

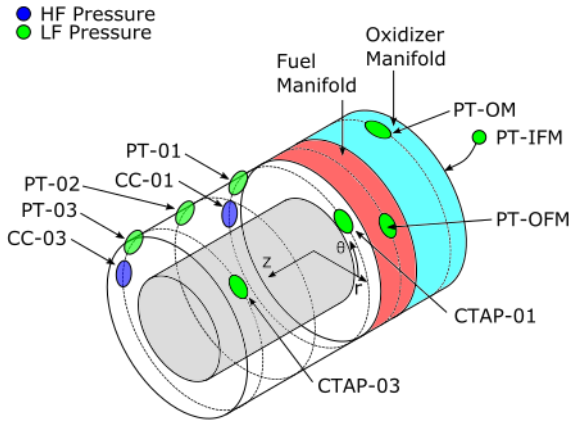

Fig. 2.3. Measurement port locations around circumference of combustor.

Table 2.1.
Coordinates of transducer port locations on combustor.

Port	Location	θ, deg.	z, mm
PT-OM	Oxidizer Manifold	90	-238
PT-01	Chamber	135	38
PT-02	Chamber	135	127
PT-03	Chamber	135	216
CC-01	Chamber	165	38
CC-03	Chamber	165	216
CTAP-01	Chamber	45	60
CTAP-03	Chamber	45	197

The wave dynamics in the chamber are visualized by directly imaging down the annulus into the injection region of the combustor. This provides information about the wave number, topology, and velocity. Images were obtained at a frame rate of 44,000 frames per second and a resolution of 256 x 256 pixels via a Phantom v411 CMOS camera. The camera was set up to the side of the engine and viewed the annulus through a mirror that was directly downstream of the RDE exhaust.

2.5 PIV System

Time-resolved PIV measurements of axial and circumferential velocity fluctuations were performed immediately downstream of the back pressure nozzle at the exit of the combustion chamber. Figure 2.4 shows the diagnostics configuration for applying PIV to this experiment, and Fig. 2.5 shows an image taken of the RDE during operation while PIV measurements were being obtained. Laser pulses were generated by a flashlamp/diode-pumped Nd:YAG-based master oscillator power amplifier Pulse-Burst Laser (PBL) system (Spectral Energies QuasiModo). The PBL system provides a 10 ms pulse train with a doublet frequency of 100 kHz, resulting in approximately 1,000 velocity vector fields. Pulse widths are approximately 10 ns with a 1.5 μs doublet spacing. The beam was expanded and collimated via two cylindrical lenses in a cylindrical telescope arrangement with focal lengths of $f_1 = -50$ mm and $f_2 = 250$ mm. The collimated sheet was focused using two more positive cylindrical lenses with focal lengths of $f_3 = f_4 = 150$ mm. The laser sheet was focused just beyond the measurement plane to achieve near-constant laser sheet thickness in the measurement plane and avoid an increase in particle drop-out near the beam waist. The measurement plane is located at $\theta = 180°$, as shown in Fig. 2.4.

Zirconia particles with an average particle size of 200 nm from a high pressure fluidized bed particle seeder are introduced into the flow using a counter-flow injector far upstream of the test article and imaging field in the oxidizer stream. The scattered light from the particles is imaged using a Phantom v2512 CMOS camera at 200 kHz

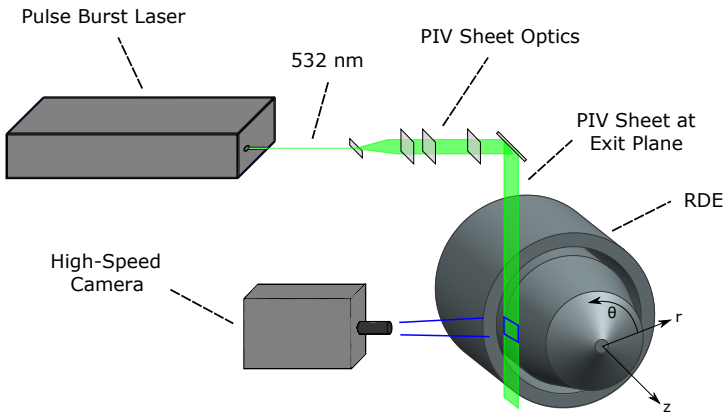

Fig. 2.4. Schematic of PIV diagnostics configuration with measurement plane centered at and tangent to $\theta = 180°$.

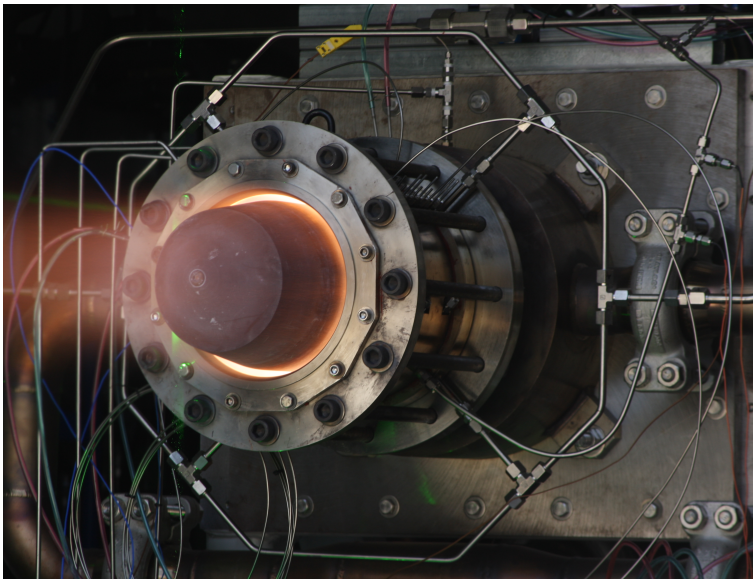

Fig. 2.5. Image showing RDE on test stand during operation. The laser beam is visible in the background, and the laser sheet for PIV measurements can be seen tangent to $\theta = 180°$.

with a 4.23 μs exposure and an active sensor size of 256 x 256 pixels. At the beginning of each test day, images were collected of a double-sided, dual-plane 3D calibration plate (LaVision Type 07). These calibration images were later used to determine the coordinate system and scaling to be used for PIV images. The scale was determined

to be approximately 7.2 pixels/mm for the PIV images used to determine the velocity measurements presented in this work.

Due to the curved geometry of the RDE center-body, the image sets collected for PIV contained glares that saturated areas of the images. Large particles that would not track were also present in many images. Further, bolt heads blocked visibility of most of the exit plane. These image characteristics needed to be masked before calculating vector fields from image pairs. Static masks were applied to mask the glare from bolt heads from the images, and dynamic masks were applied to mask the large particles.

Further image pre-processing steps were necessary to increase image quality for the PIV algorithm. First, a 5 x 5 pixel sliding window average filter was applied to all images which subtracted the calculated sliding average from each pixel. Finally, a nonlinear filter was applied to stretch each image's minimum and maximum pixel intensities to 0 and 255, respectively. A 15 x 15 pixel sliding window was used for this normalization process, thus reducing variation in laser sheet intensity throughout the image and the image set so that particles all remain of comparable intensity from one image to the next.

The LaVision commercial software (DaVis 8.4.0) was used to determine velocity vector fields for each PIV image pair. The multi-pass adaptive window offset cross-correlation algorithm was applied. Vector post-processing included a median filter with a 5 x 5 pixel sliding window that was applied three times to remove invalid vectors. If an acceptable alternative displacement correlation peak was present, it replaced the removed vector from the previous step. Calculated vectors were also removed if their correlation peak ratio was less than two, resulting in instantaneous velocity fields with empty spaces. Velocity fields consistently yielded over 90% first-choice vectors. Although an entire velocity field was obtained, only the velocity vectors along the engine centerline tangent to the RDE center-body and nearest to the exit plane were considered for velocity measurements of the detonation trailing oblique shock wave. This was to ensure that the radial component of velocity at points

considered was (near) zero, and that particles remained in the plane at all times, resulting in accurate measurements of axial and azimuthal components of velocity.

3. RESULTS AND DISCUSSION

3.1 Parametric Survey and Global Characterization of Operation

Experiments were first performed with varying mass flux, equivalence ratio, mass fraction of oxygen in air, and air inlet temperature in an attempt to find strong detonation behavior. For this parametric survey, total mass flux ranged from 50 to 550 kg/s.m^2. Equivalence ratio was varied between 0.6 and 1.7 but was near stoichiometric conditions for most cases. Gaseous oxygen was added to the main air flow for many tests, and the mass fraction of oxygen in the oxidizer flow ranged from 23.2% (air) to 33.5%. Finally, air inlet temperatures were varied between 520 K and 710 K, though no trends were discovered in the effects of air inlet temperatures. Figure 3.1 presents the reactant manifold pressures and mean chamber pressures from Test 165, illustrating a typical test sequence. Air flow is increased to the desired mass flow rate, then fuel manifolds are primed to the proper pressures for each condition. Ignition is then achieved via the pre-detonation device. Test duration is typically limited to one second or less as the RDE combustion chamber is not actively cooled.

The most sensitive tuning parameters were determined from the parametric survey to be total mass flux and oxygen enrichment mass fraction. Figure 3.2 highlights the results of this parametric survey with mass flux plotted against the oxygen mass fraction in the main oxidizer flow. The average pressure fluctuation amplitude normalized by mean chamber pressure as measured by CTAP-01 (P'/P_c) for each test is indicated by marker color. P' is calculated as the difference between the average peak differential pressure and the average valley differential pressure [55]. This parameter is determined over an averaging period later in each test to remove the effects of engine startup.

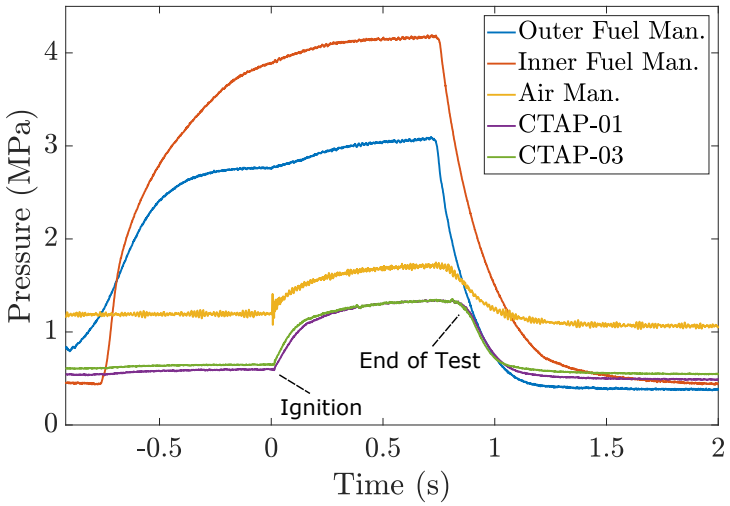

Fig. 3.1. Low frequency pressure measurements from Test 165 illustrating a typical test sequence. Air flow rate is set, then fuel manifolds are primed before ignition via the pre-detonation device. Typical test duration is less than one second as the combustor is not actively cooled.

Figure 3.2 shows that higher values of P'/P_c were only obtained for mass flux values of 300 kg/s.m^2 or higher, with the exception of two data points at 200 and 250 kg/s.m^2. Also, cases with pure air (23.2% oxygen), circled in red, all show lower values of P'/P_c. Supplemental gaseous oxygen to the main oxidizer flow (at least 26-27% by mass) was necessary to achieve higher P'/P_c values. These higher P'/P_c values typically indicated that detonation behavior was observed during the test. A general trend is observed (shown in blue in Fig. 3.2) that indicates less supplemental oxygen is necessary to obtain strong detonation behavior for higher values of total mass flux.

The highest values of P'/P_c occurred with a mass flux of approximately 300 kg/s.m^2 and a mass fraction of gaseous oxygen in the main oxidizer flow of approximately 32%. These cases sometimes resulted in single-wave behavior with frequencies in the chamber between 2 and 2.5 kHz (77-96% CJ velocity) and thus this condition (mass flux of 300 kg/s.m^2, oxygen mass fraction in oxidizer flow of 32%) was selected

to perform PIV measurements. PIV data was obtained for a similar condition (mass flux of 330 kg/s.m^2, oxygen mass fraction in oxidizer flow of 32%) that resulted in two-wave operation with a dominant frequency of 3.46 kHz (68% CJ velocity). This case, Test 165, is labeled in Fig. 3.2. The corresponding equivalence ratio was 0.95, and the air inlet temperature was 655 K.

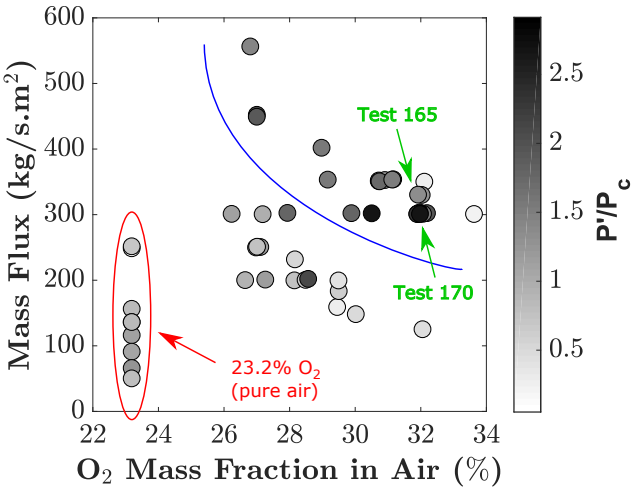

Fig. 3.2. Operating map of test conditions with corresponding P'/P_c values.

3.2 Local Heat Release Structure Analysis

High-speed images viewing the combustor annulus (downstream looking upstream) can provide information on detonation wave behavior such as wave number, topology, and velocity. Further, dominant frequency modes can be obtained from the intensity fluctuations in these images at various locations around the annulus, providing another method for verifying wave velocity information obtained from PIV and pressure data. Thus, image correction and annulus detection was performed on the collected direct, high-speed images, and a method similar to that of Bennewitz *et al.* [31] was applied to characterize global RDE behavior (number of waves, wave direction, dominant frequency modes, average wave speed) as well as instantaneous wave velocities.

The mirror that was used to image upstream into the chamber was located downstream of the RDE. As such, the mirror moved a substantial amount during every test, and the images needed to be stabilized before any analysis could be performed. First, images were converted to grayscale, as pixel intensity is the information of interest, not color. A multi-stage edge detection method as developed by Canny [56] was then applied to locate pixels along the inner and outer edges of the RDE annulus. A Taubin fit [32] was used to fit a circle to the points detected, thus determining the annulus location in each image.

Once the annulus was located, an average background subtraction was applied as presented in Bennewitz *et al.* [31]. Each pixel was then assigned an x and y Cartesian coordinate location, and subsequently an r and θ polar coordinate location, with the center ($r = 0$) located by the aforementioned annulus detection process and the θ location corresponding to the coordinate system defined in Fig. 2.3. As the radial thickness of the annulus was less than ten pixels in the obtained image sets, it was assumed that there was no radial variation in pixel intensity. The annulus was thus divided into a polar mesh with 360 azimuthal bins and only one radial bin, similar to the polar mesh shown in Fig. 1.8. An integrated (summed) pixel intensity was then determined for each bin. This integrated pixel intensity then provides time-resolved information for detonation wave location (angular position) which can be plotted on what is termed a detonation surface. A vertical line on a detonation surface at any given time intersects a number of diagonal lines corresponding to the number of waves in the chamber at that time. In this study, a negative slope for the curves on a detonation surface corresponds to clockwise rotation, aft looking forward, and a positive slope corresponds to counterclockwise rotation. The magnitude of the slope provides the detonation wave velocity, thus instantaneous wave speed can be determined for each wave throughout the duration of the image sequence.

A two-dimensional fast Fourier transformation (2D-FFT) can be performed on a detonation surface to obtain the primary spatial and temporal modes of operation [31]. An FFT of the temporal data provides the power spectrum for the frequency modes

present in the RDE. For the spatial data, an FFT provides the number of waves corresponding to the temporal modes, positive being defined as clockwise and negative as counterclockwise.

Figure 3.3 presents the detonation surface and a corresponding 2D-FFT for a time slice of Test 170. Test 170 was a case with total mass flux of 300 kg/s.m^2, equivalence ratio of 0.98, oxygen mass fraction in oxidizer flow of 30.5%, and air inlet temperature of 635 K. Figure 3.2 shows this case to have a very high value of P'/P_c equal to 2.65. The detonation surface (Fig. 3.3a) shows a single wave traveling clockwise around the chamber. The 2D-FFT (Fig. 3.3b) indicates this as well, with high-energy content corresponding to a single, clockwise-rotating wave at an operating frequency of approximately 2.3 kHz. This operating frequency corresponds to a wave velocity of 1,725 m/s (87.7% CJ velocity). Also visible on the 2D-FFT plot is the second harmonic of this mode, which appears as two clockwise rotating waves at 4.6 kHz. Lastly, the 2D-FFT plot in Fig. 3.3b indicates one weaker wave present in the chamber traveling counterclockwise at a frequency near 2.1 kHz, slower than the stronger clockwise rotating wave. Closer examination (visually) of the detonation surface shown in Fig. 3.3a shows occasional counterclockwise behavior. Further, bright spots in the detonation surface along the main clockwise rotating wave likely correspond to intersections with the weaker, counterclockwise rotating wave. These intersections break apart the stronger wave, resulting in thicker lines on the detonation surface which indicate that part of the main wave continues while a stationary combustion zone persists near the intersection location for a short amount of time.

Dynamic mode decomposition (DMD) [57] was applied to the image set for Test 170 to further analyze the periodic behavior observed in the detonation annulus. Two thousand images during this portion of the test corresponding to the primary wave rotating clockwise were analyzed. An energy spectrum from DMD was generated (Fig. 3.4) and showed the highest energy peak to correspond to 2.25 kHz, the operating frequency for the single clockwise rotating wave. Reconstructing with the modes at this frequency showed one wave (covering much more annular space than in the actual

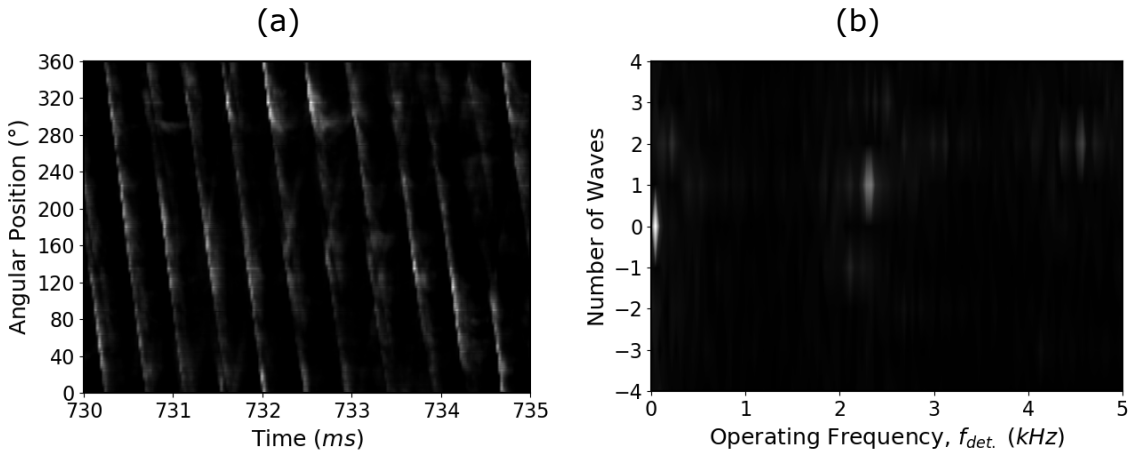

Fig. 3.3. (a) Detonation surface and (b) corresponding 2D-FFT of a time slice from Test 170 showing a single wave rotating clockwise.

images) rotating clockwise in the chamber, in agreement with conclusions from high-frequency pressure measurements and the 2D-FFT of the detonation surface in Fig. 3.3. High-energy peaks were observed clearly on the DMD energy spectrum up to the third harmonic, with each of these reconstructed modes also rotating clockwise in the RDE annulus. Figure 3.5 presents the spatial modes corresponding to the first three harmonics of the fundamental frequency. Reconstructing all modes at the fundamental frequency and higher harmonics yields one wave traveling clockwise in the chamber nearly identical to the one seen in the raw images. In addition to the fundamental frequency and higher harmonics, the energy spectrum shown in Fig. 3.4 shows high-energy content at 2.1 kHz where the 2D-FFT in Fig. 3.3b suggests the existence of a single counterclockwise-rotating wave.

At a later time in Test 170, the detonation surface and 2D-FFT shown in Fig. 3.6 indicate a change in the primary detonation mode from clockwise rotation to counter-clockwise rotation. The weaker counterclockwise rotating wave from before intersects with the stronger clockwise rotating wave and breaks it apart until it is weakened enough for the weak wave to consume more propellants and become stronger. The

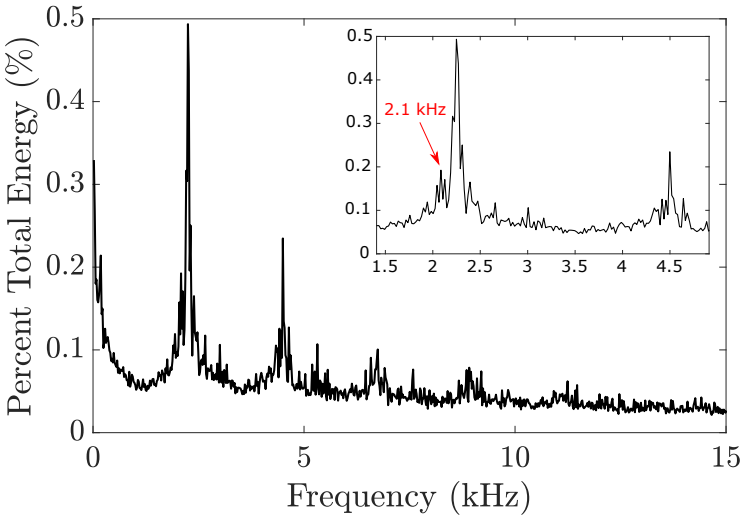

Fig. 3.4. DMD energy spectrum for an image segment in Test 170 corresponding to primary wave rotating clockwise in the chamber.

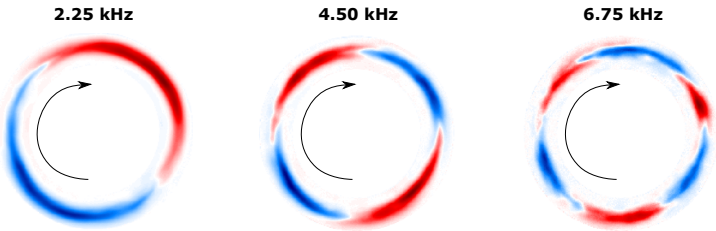

Fig. 3.5. DMD spatial modes for first three harmonics of fundamental frequency for Test 170 time slice corresponding to clockwise rotation.

two waves counter-propagate for a few cycles until only the counterclockwise wave is left. This wave now operates with a frequency in the chamber of 2.3 kHz instead of 2.1 kHz. This increased wave speed is due to the wave consuming more of the propellant in the chamber and becoming more powerful. The 2D-FFT captures both the clockwise and counterclockwise rotating modes, each with an operating frequency near 2.3 kHz corresponding to one wave in either direction. Again, this corresponds to 1,725 m/s (87.7% CJ velocity). As before, DMD is applied to isolate the spatial modes. As expected from the 2D-FFT plot, the energy spectrum (shown in Fig. 3.7) shows two spatial modes located near 2.3 kHz with high energy content. The recon-

struction of the spatial mode corresponding to the lower peak at 2.3 kHz shows one wave rotating in the counterclockwise direction.

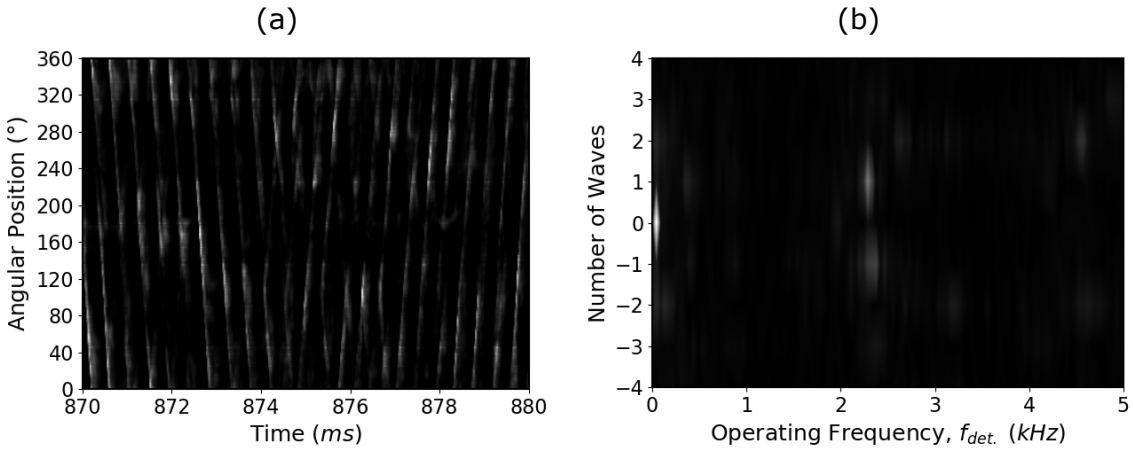

Fig. 3.6. (a) Detonation surface and (b) corresponding 2D-FFT of a time sample from Test 170 showing a single wave rotating clockwise to counterclockwise direction change.

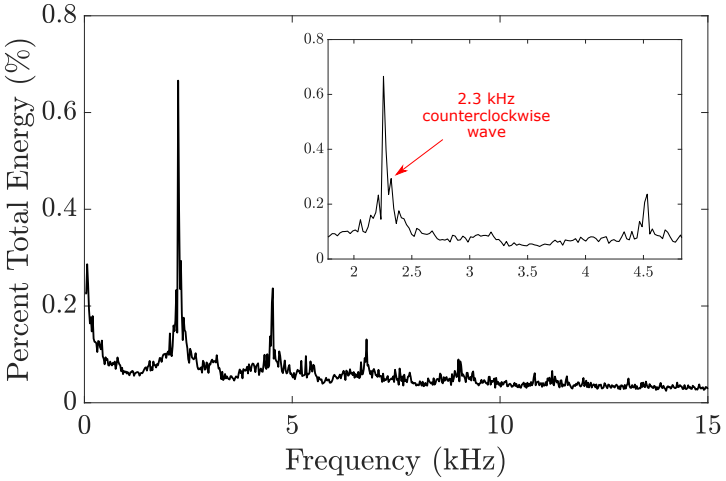

Fig. 3.7. DMD energy spectrum for an image segment in Test 170 corresponding to primary mode transition from clockwise to counterclockwise.

Finally, Fig. 3.8 shows the detonation surface and corresponding 2D-FFT plot for a time slice after the primary mode direction change previously described. The 2D-FFT (Fig. 3.8b) indicates that the highest energy mode corresponds to a single wave rotating counterclockwise at a frequency of 2.3 kHz. The 2D-FFT also indicates the presence of a single, weaker wave rotating in the clockwise direction at 2.3 kHz. This suggests that the clockwise rotating wave from the previously described time slices is still present in the chamber, even though it is not as strong as before. Again, the detonation surface (Fig. 3.8a) shows bright spots at locations along the wave, likely corresponding to intersection points with the weak clockwise rotating wave. There are certainly two waves present in the chamber throughout the duration of Test 170, as indicated by this analysis, even though the weaker wave is not often visible in the raw images or detonation surface. This could be explained by the two waves being located at different axial locations.

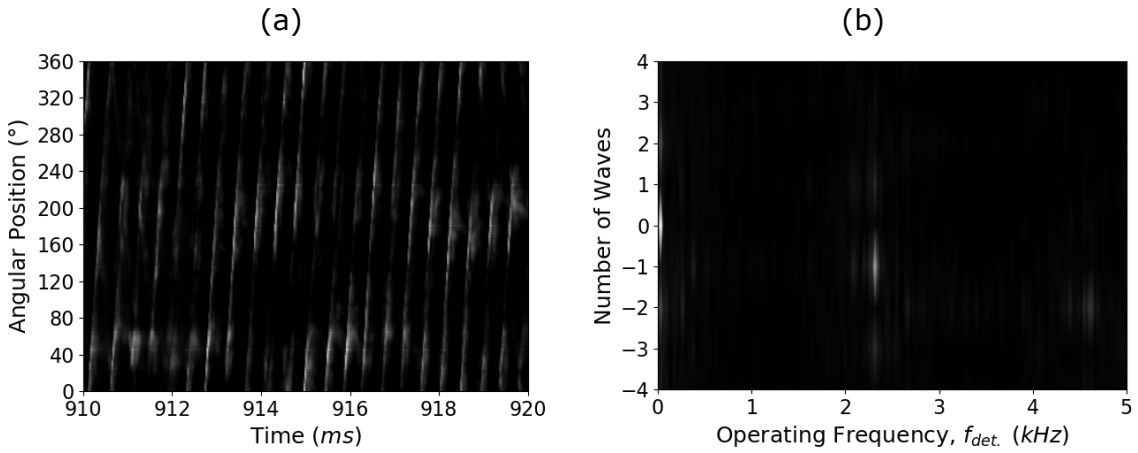

Fig. 3.8. (a) Detonation surface and (b) corresponding 2D-FFT of a time sample from Test 170 showing a single wave rotating counter-clockwise.

The detonation surface for a two-wave, clockwise rotating mode during a time slice of Test 165 is shown in the left half of Fig. 3.9. A vertical line at any time intersects two high-intensity lines with negative slope, indicating two waves rotating

clockwise. At certain locations and times on the detonation surface, faint, lower-intensity lines can be seen with positive slopes, indicating the occasional presence of a weaker detonation wave or waves traveling counterclockwise.

After performing a 2D-FFT of the detonation surface for the entire steady-state portion of Test 165, the primary mode during this test was determined to be two waves rotating clockwise. Frequency data also suggested several weaker modes corresponding to weaker detonation waves rotating counterclockwise, as previously observed on the detonation surface in Fig. 3.9. A 2D-FFT taken of a time slice that includes the presented detonation surface is shown in the right half of Fig. 3.9. Here, two waves are shown to rotate clockwise at a chamber frequency of 3.46 kHz. This frequency is not the individual frequency of each wave, but rather describes the arrival time of successive waves. Lower energy content is also visible near 3.46 kHz suggesting two weaker waves rotating counterclockwise.

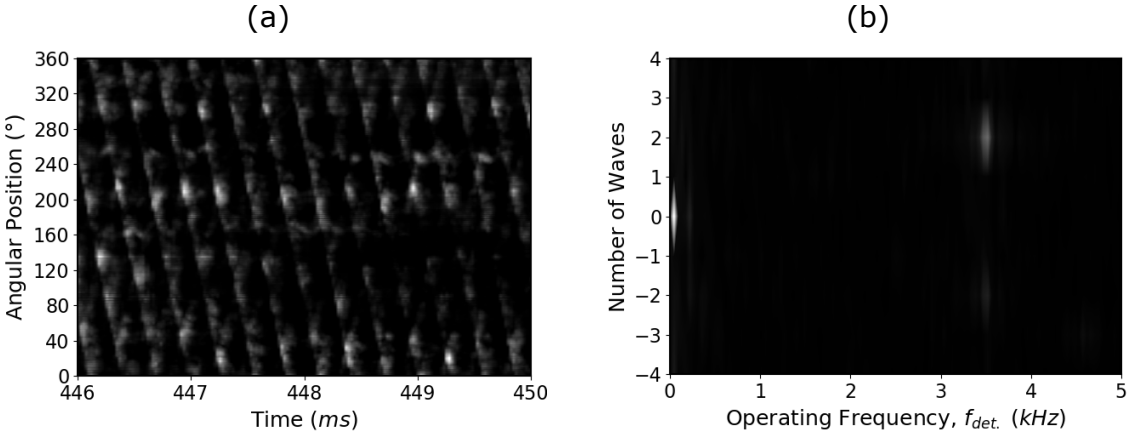

Fig. 3.9. (a) Detonation surface and (b) corresponding 2D-FFT of a time slice from Test 165 showing two waves rotating clockwise at 3.46 kHz. Low energy content in 2D-FFT is also visible for two waves rotating counterclockwise at 3.46 kHz.

DMD was also applied to an image set of seven thousand images from Test 165 to further analyze the periodic behavior observed in the detonation annulus. An

energy spectrum from DMD was generated (Fig. 3.10) and showed the highest energy peak to correspond to 3.46 kHz. Reconstructing with the modes at this frequency showed two waves (again, each covering much more annular space than in the actual images) rotating clockwise in the chamber, in agreement with conclusions from high-frequency pressure measurements and the 2D-FFT of the detonation surface. High-energy peaks were observed on the DMD energy spectrum up to the sixth harmonic, with each of these reconstructed modes also rotating clockwise in the RDE annulus. Figure 3.11 presents the spatial modes corresponding to the first five harmonics of the fundamental frequency. Reconstructing all modes at the fundamental frequency and higher harmonics yields two waves traveling clockwise in the chamber nearly identical to those seen in the raw images.

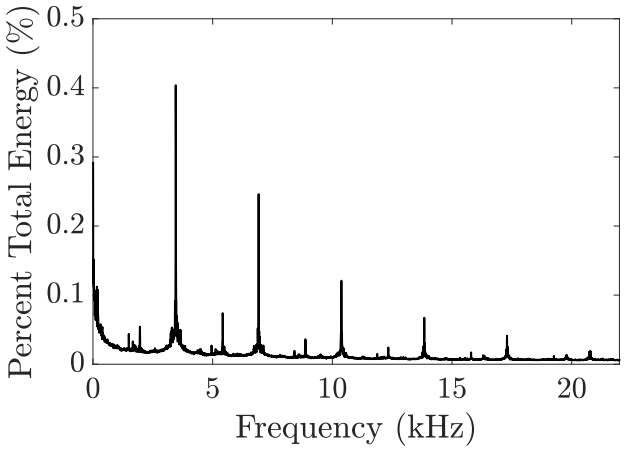

Fig. 3.10. Energy distribution of spatial modes at each frequency from DMD analysis of Test 165.

A high-energy peak was also found in the DMD energy spectrum at 1.96 kHz. The spatial mode corresponding to this frequency closely resembled that of the third harmonic (10.38 kHz). Reconstructing with the 1.96 kHz mode resulted in fluctuations rotating counterclockwise, opposite to the direction of the two stronger detonation waves. Figure 3.12 shows six sequential corrected images and a detonation surface that includes the times of these images. Two strong waves are observed to rotate

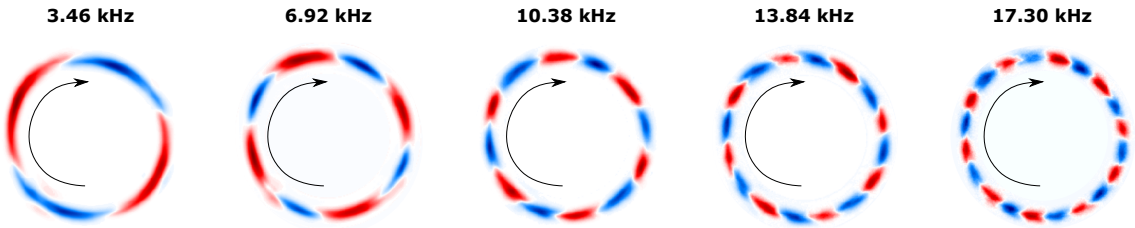

Fig. 3.11. Spatial modes for first five harmonics of fundamental frequency for Test 165.

clockwise in both the corrected images (Fig. 3.12a) and the detonation surface (Fig. 3.12b). Shown in orange on both the corrected images and the detonation surface is the development of a weaker detonation wave that is observed to propagate counter-clockwise. It is determined that the 1.96 kHz mode corresponds to the intersection of this wave with the two clockwise rotating waves, which results in much higher pixel intensity than a single propagating wave.

Also observed in Fig. 3.12 is the presence of a stationary zone of higher intensity (shown in green). This area, located near 160° in the annulus, could be an area of deflagrative burning. Further, high-frequency pressure transducers are located at $\theta = 165°$ and could be glowing in these images, though no damage was observed to CC-01 and CC-03. This area of high-intensity is likely the source of high-energy content at low frequencies in Fig. 3.10.

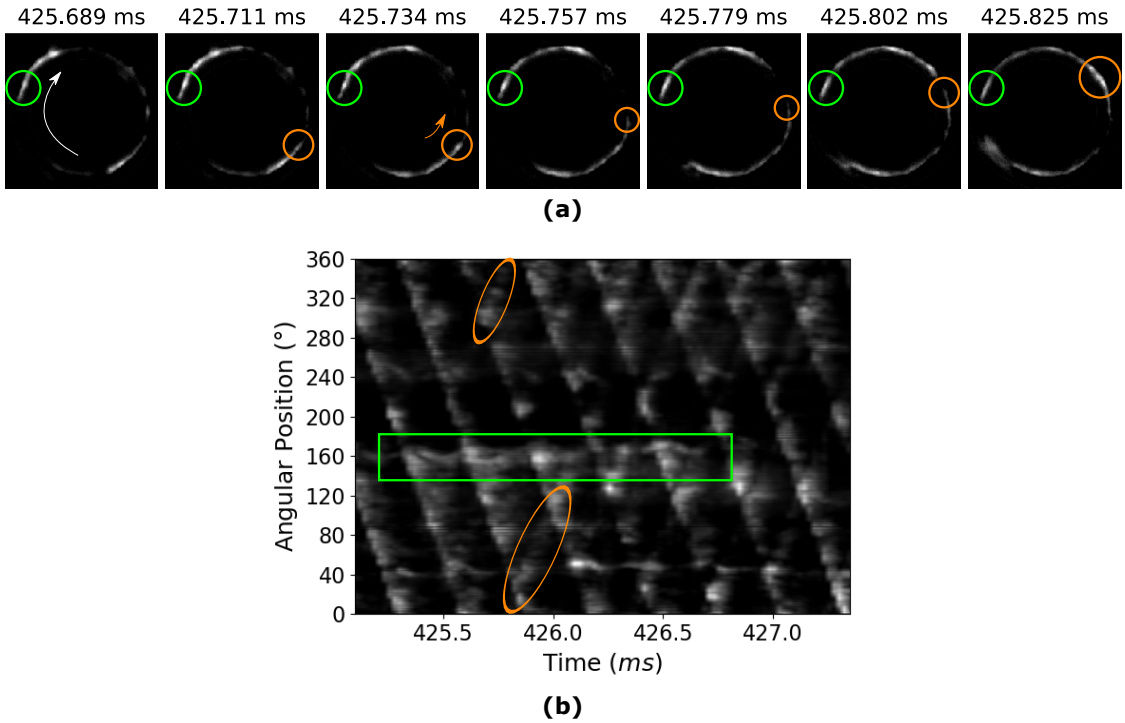

Fig. 3.12. (a) Corrected images showing two waves rotating clockwise, a stationary combustion zone (green), and a counterclockwise rotating wave (orange). (b) Detonation surface for time slice.

3.3 PIV Measurements

Figure 3.13 shows the time series for the measured axial (u_z) and azimuthal (u_θ) velocities obtained from PIV in Test 165 at 180° near the exit plane. Here, positive azimuthal velocity corresponds to flow in the direction of propagating detonation waves (clockwise for this case), while negative velocities correspond to flow opposite the direction of propagating waves (counterclockwise). The minimum axial velocity measured was approximately 800 m/s, while the maximum was near 1,400 m/s, giving a mean velocity in the time series of approximately 1,050 m/s. Initial observations of the axial velocity time series do not indicate periodic content due to the turbulent nature of the flow. Azimuthal velocity measurements, however, show strong peri-

odicity with values fluctuating between approximately -260 m/s and 135 m/s. The highest magnitudes of azimuthal velocity correspond to when the flow was traveling opposite the direction of the detonation waves. Figure 3.14 presents the time series for each velocity component corresponding to a single period of the azimuthal component, indicated by the blue lines in Fig. 3.13. Also shown are vector fields at four different times within this period. Again, a strong rise and fall of azimuthal velocity is observed during a single period, corresponding to the passing of a single detonation wave. Though a discontinuous rise in azimuthal velocity would be expected across a shock wave, a gradual rise in this component is observed. As the measurement point is located downstream of a converging-diverging nozzle, there are many combined compression/expansion processes occurring that could be causing a slower rise in azimuthal velocity.

Figure 3.15 shows measured signals during a steady-state combustion window for high-frequency chamber pressure measured by CC-01, direct high-speed image intensity fluctuations taken at the same azimuthal location as the PIV measurements ($\theta = 180°$), and the calculated azimuthal and axial velocity components at the exit plane. Also shown to the right of each time series is its corresponding power spectral density (PSD). The PSDs show excellent agreement in high-power content corresponding to the expected frequency of two, co-rotating detonation waves circumscribing the chamber (approximately 3.46 kHz). The PSD for the axial component of velocity signal does not contain as high of power at 3.46 kHz as the other signals, again attributed to turbulent effects.

Singular-Spectrum Analysis (SSA) is implemented to further explore the spectral content of the axial velocity signal. SSA decomposes a one-dimensional signal into contributing principal components (PCs) and qualitatively compares the relative significance of each PC in the reconstruction of the original signal, thus isolating higher-power constituents from noise or random fluctuations, all the while maintaining phase information throughout time [58]. SSA shows that the highest energy modes for the axial velocity signal from PIV correspond to a frequency of 3.46 kHz, in agreement

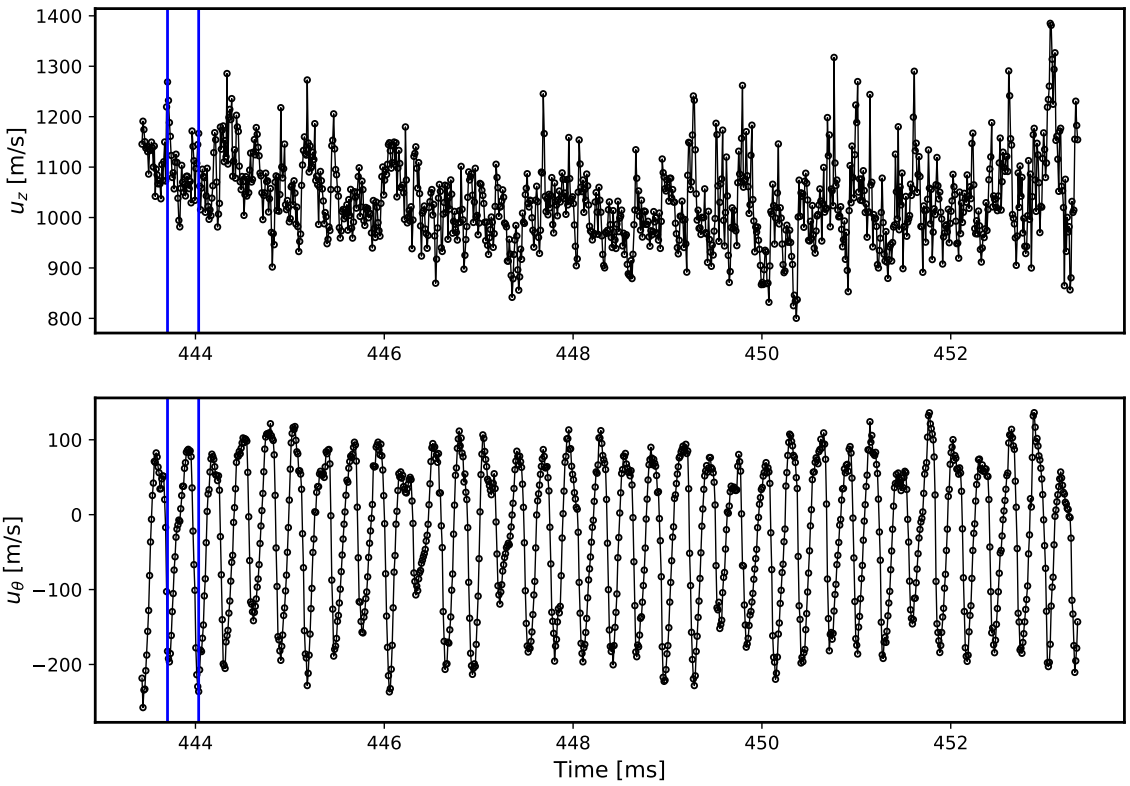

Fig. 3.13. Measured axial and azimuthal velocity near the exit plane at $\theta = 180°$. Blue lines indicate time slice shown in Fig. 3.14b.

with high-frequency pressure measurements (CC-01, CC-03), intensity fluctuations from direct high-speed imaging, and azimuthal velocity measurements.

Performing SSA on both velocity components and reconstructing the signals for frequencies near 3.46 kHz allowed for direct comparisons to be made. Figure 3.16 shows the reconstructed fluctuating signals for both components of velocity. It can be seen that the two signals seem to be nearly 180° out of phase from each other. An instantaneous phase difference was calculated using the Hilbert transform for each component and determining the difference. This instantaneous phase difference is plotted in Fig. 3.17. Axial and azimuthal velocity components are determined to be nearly 180° out of phase from each other during the time of steady-state operation

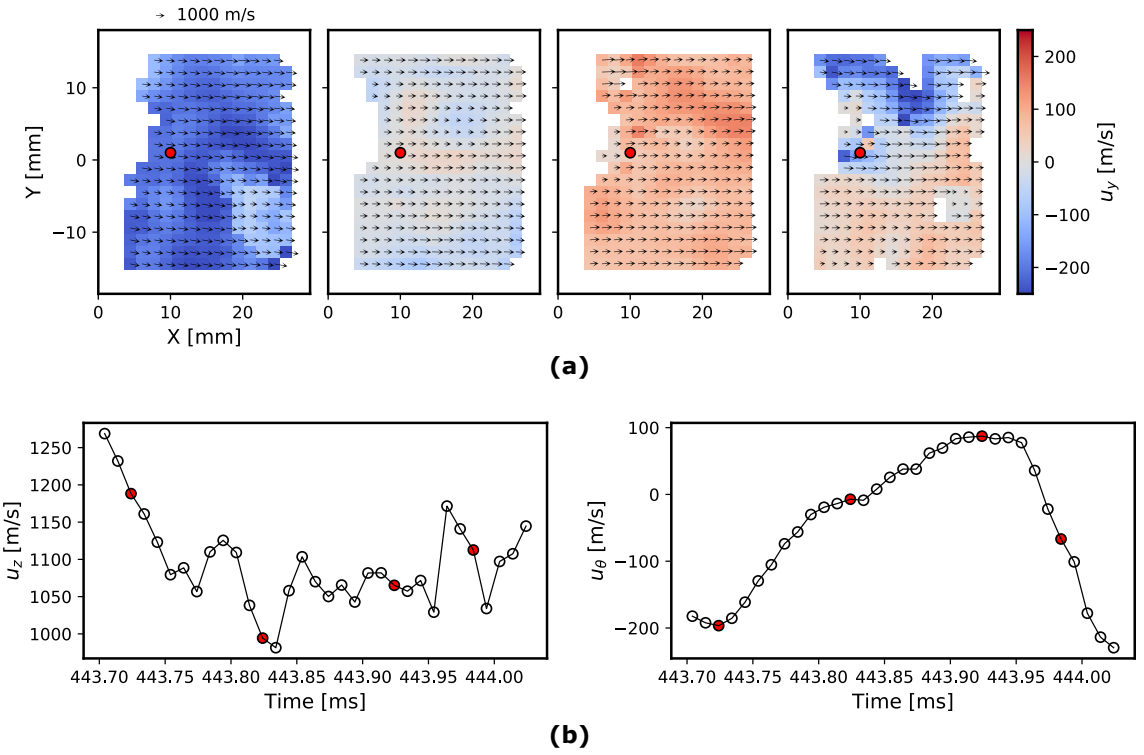

Fig. 3.14. (a) Calculated vector fields and (b) measured axial/azimuthal velocity near the exit plane over one period.

with two co-rotating detonation waves in the chamber. As a trailing oblique shock wave passes the point at the exit plane where the measurements were taken, the flow is turned in the direction of the traveling shock. Further, the local density across a shock increases so axial velocity must decrease in accordance with continuity. Shortly after the shock passes, expansion processes take place and the flow turns away from the detonation wave with a larger velocity magnitude in the counterclockwise direction. Local density falls again and thus axial velocity increases. This process repeats for each passing of a detonation wave.

SSA was also applied to high-frequency pressure measurements at the same azimuthal locations separated by a known axial distance along the chamber (CC-01 and CC-03). Reconstructed signals for CC-01 and CC-03 measurements of P'/P_c at

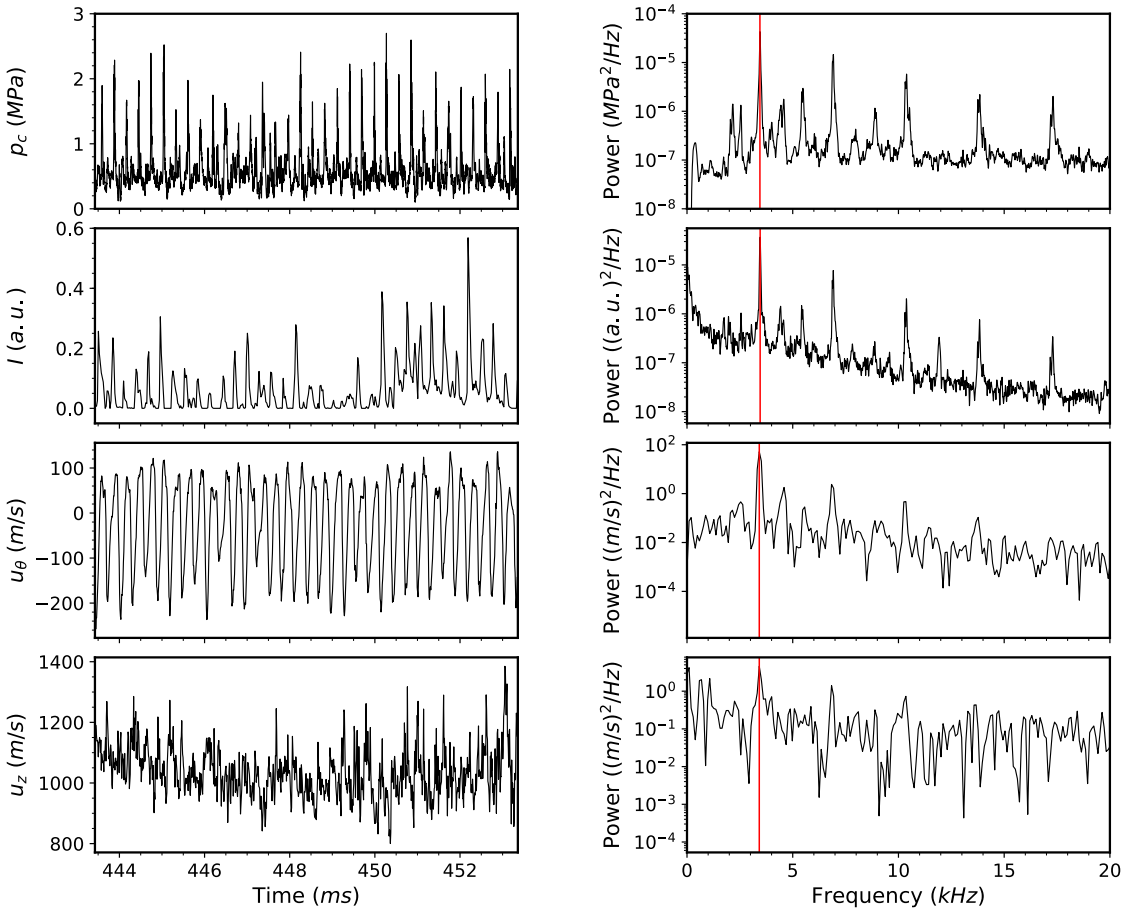

Fig. 3.15. Raw data from high-frequency pressure CC-01 (row 1, left), direct-imaging intensity (row 2, left), and azimuthal and axial components of velocity measured in PIV (rows 3 and 4, left) along with corresponding power spectral density (PSD) plots to the right with most powerful frequencies indicated by a vertical red line for each PSD.

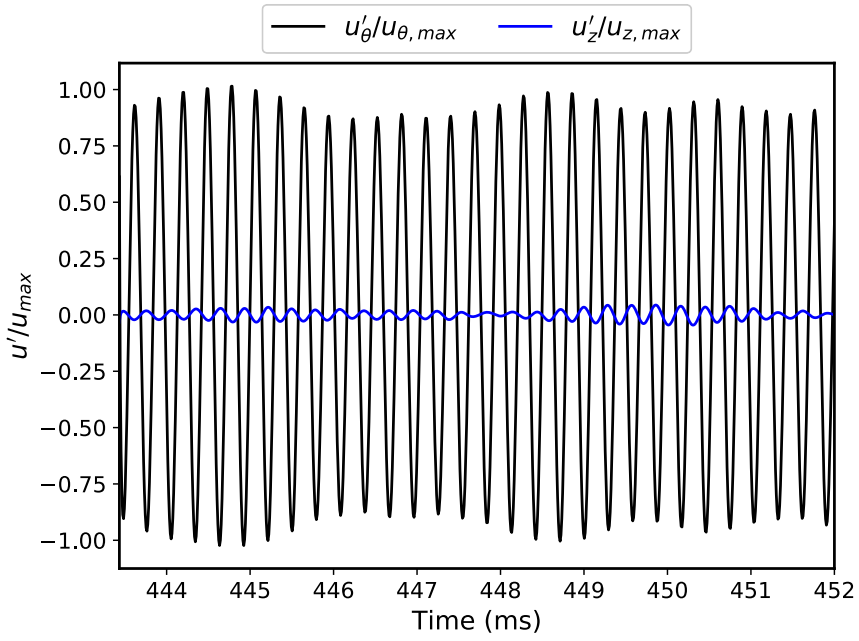

Fig. 3.16. Reconstructed fluctuation signals from SSA for frequencies near 3.46 kHz for both $u_\theta/u_{\theta,max}$ and $u_z/u_{z,max}$.

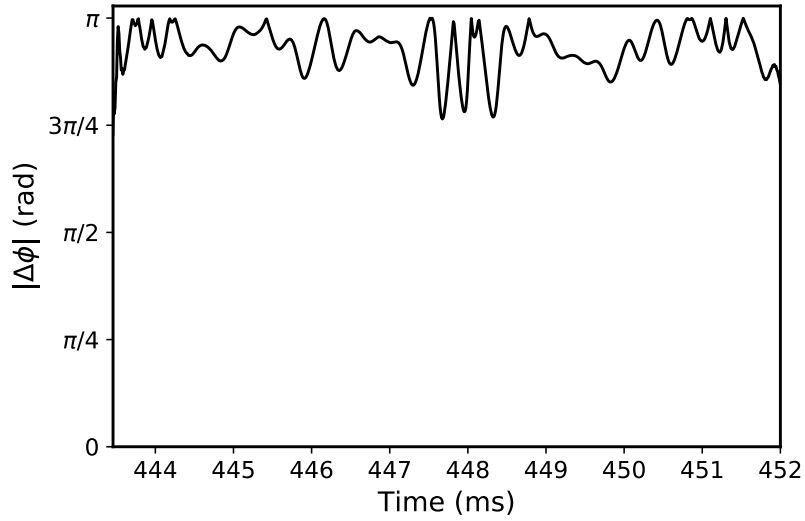

Fig. 3.17. Instantaneous phase difference between reconstructed fluctuation signals from SSA for frequencies near 3.46 kHz for $u_\theta/u_{\theta,max}$ and $u_z/u_{z,max}$.

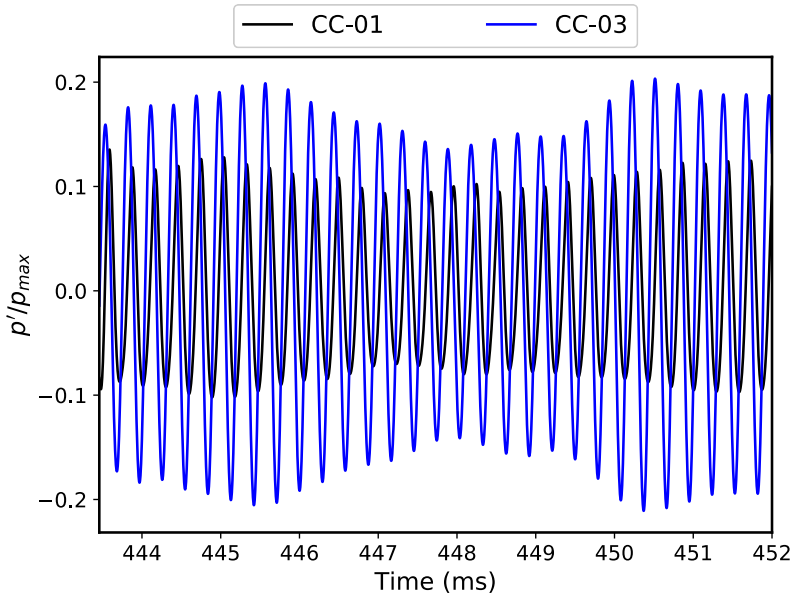

Fig. 3.18. Reconstructed fluctuation signals from SSA for frequencies near 3.46 kHz for p'/p_{max} corresponding to both CC-01 and CC-03 measurements.

the 3.46 kHz modes are shown in Fig. 3.18. The sonic speed in the chamber was approximated throughout time based on the difference in time between peaks in the reconstructed signals for CC-01 and CC-03. These approximated values of sonic velocity are presented in Fig. 3.19. Knowing sonic velocity and the detonation velocity, an approximate shock angle can be calculated using basic trigonometric relations. Figure 3.20 shows the approximated shock angles for this case, with angles varying from near 32° to above 34°.

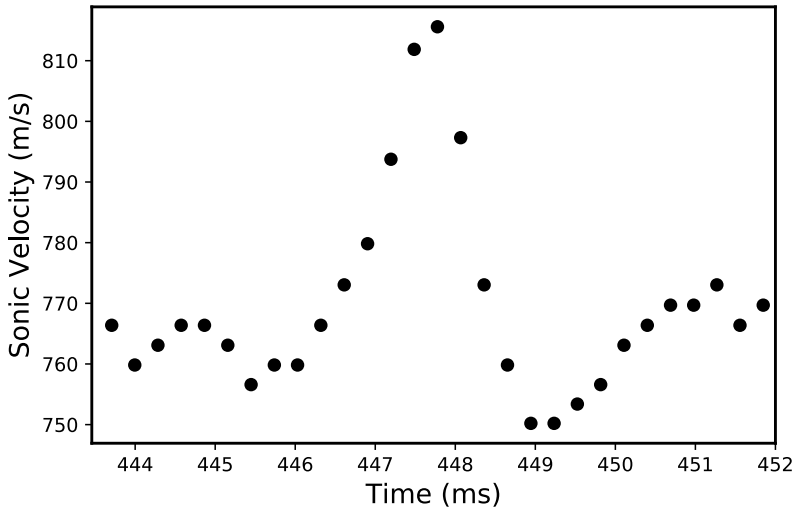

Fig. 3.19. Mean sonic velocities in chamber section between CC-01 and CC-03.

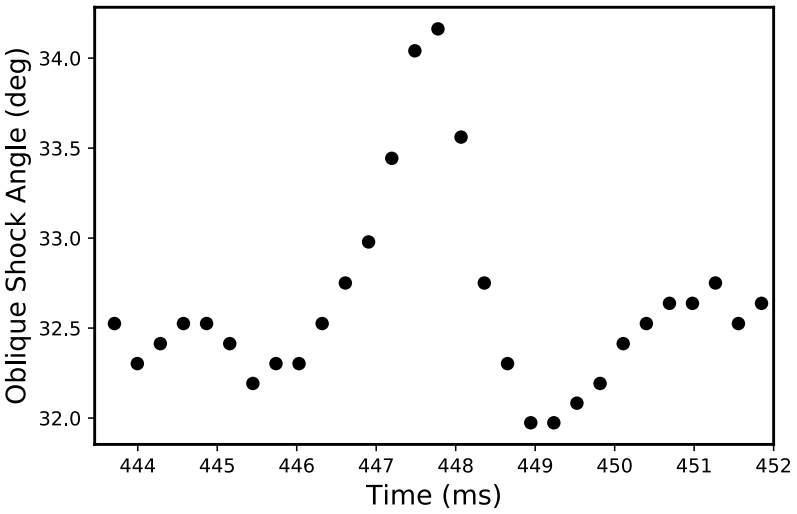

Fig. 3.20. Approximated oblique shock angles based on calculated mean sonic velocities and detonation velocities in the chamber.

4. SUMMARY

Experiments were performed with a 23.9 cm RDE with natural gas-air propellants. A parametric survey concluded that supplemental oxygen was necessary to achieve strong detonative behavior and that a mass flux of at least 300 kg/s.m^2 was also required. High-frequency pressure measurements were obtained, and chemiluminescence imaging of the detonation annulus and PIV at the exit plane were performed for a test case with 330 kg/s.m^2 mass flux and 32% oxygen (by mass) in main oxidizer flow at stoichiometric conditions. All measurements indicated two strong detonation waves rotating clockwise around the annulus with frequency of 3.46 kHz, corresponding to 68% CJ velocity.

Further analysis of the chemiluminescence images suggested weaker waves present in the chamber traveling in the opposite direction of the two strong detonation waves. A detonation surface was generated and analyzed by performing a 2D-FFT. This analysis showed two strong waves rotating clockwise, as well as occasional, weaker detonation waves rotating counterclockwise. DMD analysis of the chemiluminescence images showed the two clockwise rotating waves to be the highest energy mode. DMD also allowed for the identification of a 1.96 kHz mode in the chamber that is attributed to the intersections of weaker, counterclockwise rotating detonation waves with the two clockwise co-rotating waves.

PIV measurements at the exit plane show strong periodic behavior in the azimuthal velocity component which fluctuates with a frequency of 3.46 kHz, corresponding to two clockwise rotating trailing oblique shock waves associated with the detonation waves in the chamber. SSA showed relatively high energy frequency content for the axial velocity component at 3.46 kHz. Phase information for the two components of velocity from PIV showed the two signals to be nearly 180° out of phase. This was attributed to the rise in density across a shock and the necessary

decrease in axial velocity for continuity to be satisfied, followed by the immediate fall in density due to expansion processes and a corresponding increase in axial velocity.

SSA was also applied to high-frequency pressure measurements at the same azimuthal locations separated by a known axial distance along the chamber (CC-01 and CC-03). The mean sonic speed in the chamber was approximated throughout time based on the difference in time between peaks in P'/P_c for the CC-01 and CC-03 signals reconstructed at the 3.46 kHz modes. These sonic speeds were then used to approximate the angle of the trailing oblique shocks associated with each detonation wave in the chamber. This method for measuring oblique shock angles in the chamber of an RDE could provide insight into wave structure in the combustion annulus.

REFERENCES

REFERENCES

[1] P. Wolański, "Application of the Continuous Rotating Detonation to Gas Turbine," *Applied Mechanics and Materials*, vol. 782, pp. 3–12, 2015.

[2] C. A. Nordeen, "Thermodynamics of a Rotating Detonation Engine," Ph.D. dissertation, University of Connecticut, 2013.

[3] F. K. Lu and E. M. Braun, "Rotating Detonation Wave Propulsion: Experimental Challenges, Modeling, and Engine Concepts," *Journal of Propulsion and Power*, vol. 30, no. 5, pp. 1125–1142, 2014.

[4] K. M. Pandey and P. Debnath, "Review on Recent Advances in Pulse Detonation Engines," *Journal of Combustion*, vol. 2016, 2016.

[5] G. D. Roy, S. M. Frolov, A. A. Borisov, and D. W. Netzer, "Pulse detonation propulsion: Challenges, current status, and future perspective," *Progress in Energy and Combustion Science*, 2004.

[6] F. A. Bykovskii, S. A. Zhdan, and E. F. Vedernikov, "Continuous Spin Detonations," *Journal of Propulsion and Power*, vol. 22, no. 6, pp. 1204–1216, 2006.

[7] K. Kailasanath, "Recent Developments in the Research on Rotating-Detonation-Wave Engines," *55th AIAA Aerospace Sciences Meeting*, January 2017.

[8] J. H. S. Lee and M. I. Radulescu, "On the Hydrodynamic Thickness of Cellular Detonations," *Combustion, Explosion, and Shock Waves*, vol. 41, no. 6, pp. 745–765, 2005.

[9] M. I. Radulescu and J. H. S. Lee, "The Failure Mechanism of Gaseous Detonations: Experiments in Porous Wall Tubes," *Combustion and Flame*, vol. 131, pp. 29–46, 2002.

[10] I. Walters, C. L. Journell, A. Lemcherfi, R. Gejji, S. Heister, and C. D. Slabaugh, "Parametric Survey of a Natural Gas-Air Rotating Detonation Engine at Elevated Pressure," *57th AIAA Aerospace Sciences Meeting*, January 2019.

[11] M. Kaneshige and J. Shepherd, "Detonation Database," GALCIT, Technical Report FM97-8, Tech. Rep., July 1997. [Online]. Available: http://shepherd.caltech.edu/detn_db/html/db_4.html

[12] C. A. Stevens, J. L. Hoke, and F. R. Schauer, "Propane-Air Cell Size Correlation to Temperature and Pressure," *54th AIAA Aerospace Sciences Meeting*, January 2016.

[13] P. A. Bauer, H. N. Presles, O. Heuze, and C. Brochet, "Measurement of cell lengths in the detonation front of hydrocarbon oxygen and nitrogen mixtures at elevated initial pressures," *Combustion and Flame*, vol. 64, pp. 113–123, 1986.

[14] S. Siwiec and P. Wolański, "Detonation cell structure in CH_4-air mixture at high pressure," *archivum combustionis*, vol. 4, no. 3, pp. 249–253, 1984.

[15] B. V. Voitsekhovskii, "Stationary Detonation," *Doklady Akademii Nauk UzSSR*, vol. 129, no. 6, pp. 1254–1256, 1959.

[16] ——, "Stationary Spin Detonation," *Soviet Journal of Applied Mechanics and Technical Physics*, no. 3, pp. 157–164, 1960.

[17] J. H. S. Lee, *The Detonation Phenomenon*, 1st ed. Cambridge University Press, 2008.

[18] J. A. Nicholls, R. E. Cullen, and T. C. Adamson Jr., "The Feasibility of a Rotating Detonation Wave Rocket Motor: Final Report," University of Michigan, Tech. Rep. ORA Report 05179, 1964.

[19] F. A. Bykovskii, I. D. Klopotov, and V. V. Mitrofanov, "Spin detonation of gases in a cylindrical chamber," *Akademia Nauk SSSR Doklady*, vol. 224, no. 5, pp. 1038–1041, 1975.

[20] Bykovskii, F A and Zhdan, S A and Vedernikov, E F and Samsonov, A N, "Scaling Factor in Continuous Spin Detonation of Syngas-Air Mixtures," *Combustion, Explosion, and Shock Waves*, vol. 53, no. 2, pp. 187–198, 2017.

[21] B. A. Rankin, D. R. Richardson, A. W. Caswell, A. G. Naples, J. L. Hoke, and F. R. Schauer, "Chemiluminescence imaging of an optically accessible non-premixed rotating detonation engine," *Combustion and Flame*, pp. 12–22, 2017.

[22] V. Anand, A. S. George, R. Driscoll, and E. Gutmark, "Characterization of instabilities in a Rotating Detonation Combustor," *International Journal of Hydrogen Energy*, vol. 40, pp. 16 649–16 659, 2015.

[23] J. C. Shank, P. I. King, J. Karnesky, F. R. Schauer, and J. L. Hoke, "Development and Testing of a Modular Rotating Detonation Engine," *50th AIAA Aerospace Sciences Meeting*, January 2012.

[24] M. L. Fotia, F. Schauer, T. Kaemming, and J. Hoke, "Experimental Study of the Performance of a Rotating Detonation Engine with Nozzle," *Journal of Propulsion and Power*, vol. 32, no. 3, pp. 674–681, 2016.

[25] B. A. Rankin, J. R. Codoni, K. Y. Cho, J. L. Hoke, and F. R. Schauer, "Investigation of the structure of detonation waves in a non-premixed hydrogen–air rotating detonation engine using mid-infrared imaging," *Proceedings of the Combustion Institute*, vol. 37, pp. 3479–3486, 2019.

[26] W. Y. Peng, S. J. Cassady, C. L. Strand, C. S. Goldenstein, R. M. Spearrin, C. M. Brophy, J. B. Jeffries, and R. K. Hanson, "Single-ended mid-infrared laser-absorption sensor for time-resolved measurements of water concentration and temperature within the annulus of a rotating detonation engine," *Proceedings of the Combustion Institute*, vol. 37, pp. 1435–1443, 2019.

[27] D. L. Depperschmidt, J. R. Tobias, R. S. Miller, M. Uddi, A. K. Agrawal, and J. B. Stout, "Time-Resolved PIV Diagnostics to Measure Flow Field Exiting Methane-Fueled Rotating Detonation Combustor," *57th AIAA Aerospace Sciences Meeting*, January 2019.

[28] I. Walters, C. L. Journell, A. Lemcherfi, R. Gejji, S. Heister, and C. D. Slabaugh, "Experimental Investigation of a Piloted, Natural Gas-Air Rotating Detonation Wave Combustor," *54th Joint Propulsion Conference*, July 2018.

[29] L. Wei, Z. Jin, L. Shijie, and L. Zhiyong, "An experimental study on CH_4/O_2 continuously rotating detonation wave in a hollow combustion chamber," *Experimental Thermal and Fluid Science*, vol. 62, pp. 122–130, 2015.

[30] J. Kindracki, "Experimental research on rotating detonation in liquid fuel-gaseous air mixtures," *Aerospace Science and Technology*, vol. 43, pp. 445–453, 2015.

[31] J. W. Bennewitz, B. R. Bigler, W. A. Hargus, S. A. Danczyk, and R. D. Smith, "Characterization of Detonation Wave Propagation in a Rotating Detonation Rocket Engine using Direct High-Speed Imaging," *54th AIAA Joint Propulsion Conference*, July 2018.

[32] G. Taubin, "Estimation of Planar Curves, Surfaces, and Nonplanar Space Curves Defined by Implicit Equations with Applications to Edge and Range Image Segmentation," *IEEE Transactions on Pattern Analysis and Machine Intelligence*, vol. 13, pp. 1115–1138, 1991.

[33] J. Kindracki, P. Wolański, and Z. Gut, "Experimental research on the rotating detonation in gaseous fuels–oxygen mixtures," *Shock Waves*, vol. 21, pp. 75–84, 2011.

[34] J. Tobias, D. Depperschmidt, C. Welch, R. Miller, M. Uddi, A. K. Agrawal, and R. Daniel, Jr., "OH* Chemiluminescence Imaging of the Combustion Products From a Methane-Fueled Rotating Detonation Engine," *Journal of Engineering for Gas Turbines and Power*, vol. 141, 2019.

[35] C. S. Goldenstein, C. A. Almodóvar, J. B. Jeffries, R. K. Hanson, and C. M. Brophy, "High-bandwidth scanned-wavelength-modulation spectroscopy sensors for temperature and H_2O in a rotating detonation engine," *Measurement Science and Technology*, vol. 25, no. 10, 2014.

[36] C. J. McGahan, B. A. Tom, A. W. Caswell, J. R. Gord, F. Schauer, and J. Hoke, "Exhaust Gas Analysis of a Rotating Detonation Engine using Tunable Diode Laser Absorption Spectroscopy," *52nd Aerospace Sciences Meeting*, January 2014.

[37] L. Mach, "Über die Sichtbarmachung von Luftstromlinien," *Zeitschrift für Luftschiffahrt und Physik der Atmosphäre*, vol. 15, no. 6, pp. 129–139, 1896.

[38] L. Prandtl, "Über Flüssigkeitsbewegung bei sehr kleiner Reibung," *Verhandlungen des III. Internationalen Mathematiker Kongresses, Heidelberg*, pp. 484–491, 8-13 August 1904.

[39] M. Raffel, C. E. Willert, F. Scarano, C. J. Kähler, S. T. Wereley, and J. Kompenhans, *Particle Image Velocimetry: A Practical Guide*, 3rd ed. Springer, 2018.

[40] R. J. Adrian and J. Westerweel, *Particle Image Velocimetry*, 1st ed. Cambridge University Press, 2011.

[41] *DaVis 8.4 FlowMaster Product-Manual*, LaVision GmbH, Anna-Vandenhoeck-Ring 19, D-37081 Göttingen, Germany, January 20, 2017.

[42] B. Thurow, N. Jiang, and W. Lempert, "Review of ultra-high repetition rate laser diagnostics for fluid dynamic measurements," *Measurement Science and Technology*, vol. 24, no. 1, 2013.

[43] M. P. Wernet and A. B. Opalski, "Development and Application of a MHz Frame Rate Digital Particle Image Velocimetry System," *AIAA Aerodynamic Measurement Technology and Ground Testing Conf.*, 2004.

[44] M. P. Wernet, "Temporally resolved PIV for space-time correlations in both cold and hot jet flows," *Measurement Science and Technology*, vol. 18, no. 7, 2007.

[45] B. Brock, R. H. Haynes, B. S. Thurow, G. Lyons, and N. E. Murray, "An examination of MHz rate PIV in a heated supersonic jet," *52nd AIAA Aerospace Sciences Meeting*, January 2014.

[46] S. J. Beresh, J. F. Henfling, R. W. Spillers, and S. M. Spitzer, "'Postage-stamp PIV': small velocity fields at 400 kHz for turbulence spectra measurements," *Measurement Science and Technology*, vol. 29, no. 3, 2018.

[47] J. D. Miller, J. R. Gord, T. R. Meyer, M. N. Slipchenko, J. G. Mance, and S. Roy, "Development of a diode-pumped, 100-ms quasi-continuous burst-mode laser for high-speed combustion diagnostics," *30th AIAA Aerodynamic Measurement Technology and Ground Testing Conference*, June 2014.

[48] J. D. Miller, N. Jiang, M. N. Slipchenko, J. G. Mance, T. R. Meyer, S. Roy, and J. R. Gord, "Spatiotemporal analysis of turbulent jets enabled by 100-kHz, 100-ms burst-mode particle image velocimetry," *Experiments in Fluids*, vol. 57, 2016.

[49] M. E. Smyser, K. A. Rahman, M. N. Slipchenko, S. Roy, and T. R. Meyer, "Compact burst-mode Nd:YAG laser for kHz-MHz bandwidth velocity and species measurements," *Optics Letters*, vol. 43, no. 4, 2018.

[50] C. M. Ehresman, "History of the Maurice J. Zucrow Laboratories." [Online]. Available: https://engineering.purdue.edu/Zucrow/about-us/history

[51] T. L. Pourpoint, S. E. Meyer, and C. M. Ehresman, "Propulsion Test Facilities at the Purdue University Maurice J. Zucrow Laboratories," *43rd AIAA/ASME/SAE/ASEE Joint Propulsion Conference & Exhibit*, July 2007.

[52] S. E. Meyer, S. D. Heister, C. Slabaugh, R. P. Lucht, A. Pratt, R. M. Gejji, M. Bedard, and A. Lemcherfi, "Design and Development of the High Pressure Combustion Laboratory at Purdue University," *53rd AIAA/SAE/ASEE Joint Propulsion Conference*, July 2017.

[53] ISO 9300, "ISO 9300: Measurement of gas flow by means of critical flow," 2005.

[54] E. W. Lemmon, and Ian H. Bell, M. L. Huber, and M. O. McLinden, "NIST Standard Reference Database 23: Reference Fluid Thermodynamic and Transport Properties-REFPROP, Version 10.0, National Institute of Standards and Technology," 2018. [Online]. Available: https://www.nist.gov/srd/refprop

[55] K. Schwinn, R. Gejji, B. Kan, S. Sardeshmukh, S. Heister, and C. D. Slabaugh, "Self-sustained, high-frequency detonation wave generation in a semi-bounded channel," *Combustion and Flame*, vol. 193, pp. 384–396, 2018. [Online]. Available: https://doi.org/10.1016/j.combustflame.2018.03.022

[56] J. F. Canny, "A Computational Approach to Edge Detection," *IEEE Transactions on Pattern Analysis and Machine Intelligence*, vol. PAMI-8, no. 6, pp. 679–698, 1986.

[57] P. Schmid, "Dynamic mode decomposition of numerical and experimental data," *Journal of Fluid Mechanics*, vol. 656, pp. 5–28, 2010.

[58] R. Vautard, P. Yiou, and M. Ghil, "Singular-spectrum analysis: A toolkit for short, noisy chaotic signals," *Physica D*, vol. 58, pp. 95–126, 1992.

VITA

VITA

Christopher Lee Journell was born to Ron and Jackie Journell on August 16, 1993 and was raised in Salem, Indiana. He graduated from Purdue University in West Lafayette, Indiana with a Bachelor of Science in Aeronautical and Astronautical Engineering (BSAAE) in December of 2016. Throughout his undergraduate career, he also completed four Co-Op terms with GE Aviation in Evendale, Ohio and Lynn, Massachusetts. Upon completion of his BSAAE, he continued on at Purdue University conducting research on the development and application of high-speed diagnostics in rotating detonation engines. On January 5, 2019, he married Claire Elizabeth Journell.